TECHNISCHE MECHANIK
an open access journal

journal homepage: www.ovgu.de/techmech

Tech. Mech., Vol. 42, Is. 1, (2022), 14–35

Received: 21.05.2022
Accepted: 26.08.20222
Available online: 01.09.2022

Benchmarking of glyph-based visualization concepts for fourth-order tensors using von Mises plasticity and Ogden hyperelasticity

Chiara Hergl[1]*, Christian Silbermann[2], Thomas Nagel[2], and Gerik Scheuermann[1]

[1] Leipzig University, Institute of Computer Science, Augustusplatz 10, 04109 Leipzig, Germany
[2] Technische Universität Bergakademie Freiberg, Geotechnical Institute, Gustav-Zeuner-Straße 1, 09599 Freiberg, Germany

Abstract: The visualization of higher-order tensors receives increasing attention, because they carry important information in many areas of physics, especially mechanics, as well as earth sciences or medicine. Higher-order tensors challenge any visualization method due to their higher number of coefficients compared to scalars, vectors, or second-order tensors. In this article, we focus on the stiffness tensor and compare four glyph-based visualization methods. The first glyph exploits the deformation modes, the second one the plane waves, the third one the anisotropy types, and the last one exploits the uniaxial stiffness (or compliance) of the material. The visualization methods are compared using two different examples. The first example is an elasto-plastic, thick-walled, hollow sphere under pressure and the second example describes an indentation test, where a spherical indenter is pressed into a soft biological material. Both advantages and drawbacks of the selected methods are discussed. Special emphasis is placed on the case of a singular stiffness tensor indicating a type of instability. As it is shown, the visualization method must be chosen with care to extract the relevant information from the tensor in a reliable way.

Keywords: glyph-based visualization, stiffness tensor, tensor field, von Mises plasticity, hyperelasticity, plane waves, acoustic tensor

1 Introduction

The tissue engineering of artificial muscles using electroactive polymers, the analysis of seismic activities in the earth's crust, the adaptation of bone around an endoprosthesis as well as the deformation of biological tissues and geomaterials alike do not seem to have much in common at a first glance. But all of these problems are related to materials with direction-dependent properties that may change over time. Furthermore, the analysis of these materials is central to the success of each of the above applications. The mechanical properties of such materials can be described by the fourth-order three-dimensional stiffness tensor. Due to the complexity of higher-order tensors there are only a few visualization methods available to analyze them. In the common case of major and minor symmetries of the stiffness tensor, the number of independent coefficients reduces from 81 to 21 (cf. section 2). These symmetries can be exploited for the decomposition of the tensor using specific methods (cf. section 3).

This work analyzes two specific examples presented in section 4. The first one is a small-strain elasto-plastic data set with spherical symmetry derived analytically. As a consequence of the assumed ideal plastic behavior, the stiffness tensor becomes singular, still it is physically meaningful. When applying visualization methods care must be taken, especially if the (non-existing) inverse tensor is involved. Even though, it does not exist analytically, numerically it can be calculated. This is a consequence of calculating the coefficients of the stiffness tensor with finite precision. This peculiarity allows us to test the sensitivity of the four visualization methods with respect to singular stiffness tensors, which can be of practical concern when dealing with any kind of instability problem. The second example is given by a non-linear simulation of an indentation test of a soft biological material using a finite-strain, hyperelastic Ogden-type constitutive model. Here, the indentation causes deformation-induced anisotropy, and the stiffness tensor is regular. For each of these data sets four different glyph-based methods are applied and discussed in section 5. Three of the methods come from the visualization community and one from the application side. Finally, in section 6 we discuss advantages and drawbacks of the different methods for different use cases.

The goal of this work is the presentation of different glyph-based visualization methods to analyze the stiffness tensor. Therefore, the methods are described using single glyphs. However, in continuum physics, tensors are *field* quantities. Consequently, their visualization results in glyph *fields*. Thus, the presented glyphs are tested on two different stiffness tensor field data sets. This work will discuss different scenarios to give an initial assessment of the usefulness of the four glyphs. However, it will not give a recommendation which glyph is the best because the usefulness of each glyph is strongly dependent on the application.

The following **conventions** are used in this work: In the symbolic tensor notation $\boldsymbol{d}, \boldsymbol{S}, \mathbb{C}$ represent tensors of first, second and fourth order, respectively. In the index notation the index variables $i, j, k, l, \ldots$ stand for the indices of any orthonormal basis (e. g. Cartesian coordinates x, y, z, spherical coordinates r, θ, φ, or principal coordinates $1, 2, 3,$) and Einstein's summation convention holds. The indices $\alpha, \beta \in [1, 2, \ldots]$ are used as counter, e. g. for a numerical coordinate grid. Any upright indices, e. g. iso, are identifiers. The operators $\cdot$ and : denote the single and double contraction with $\boldsymbol{a} \cdot \boldsymbol{b} = a_i b_i$, $\boldsymbol{A} : \boldsymbol{B} = A_{ij} B_{ij}$, $\otimes$ denotes the dyadic product.

* E-mail address: hergl@informatik.uni-leipzig.de
doi: 10.24352/UB.OVGU-2022-058

2 Continuum Mechanical Basics and Stiffness Tensor

The examples used in this work require knowledge of mechanical relations, which are briefly described in the following paragraph. We will consider finite deformations and use the classical notion of non-linear continuum mechanics, see e. g. Holzapfel (2000). Starting from the second-order *deformation gradient* $\boldsymbol{F}$, the right Cauchy-Green tensor is obtained as

$$\boldsymbol{C} = \boldsymbol{F}^{\mathrm{T}} \cdot \boldsymbol{F} \,. \tag{1}$$

Since this tensor is different from zero even in the absence of any deformation, it is beneficial to introduce strain-type measures such as the *Green-Lagrange strain tensor*

$$\boldsymbol{E} = \frac{1}{2}(\boldsymbol{C} - \boldsymbol{I}) \,, \tag{2}$$

where $\mathbf{I}$ is the identity tensor with $I_{ij} = \delta_{ij}$. With the vector $\boldsymbol{u}$ describing the displacement of some material point, the displacement gradient $\boldsymbol{H}$ can be used to express the Green-Lagrange strain tensor $\boldsymbol{E}$ in the following way:

$$\boldsymbol{H} = \mathrm{Grad}(\boldsymbol{u}) = \boldsymbol{F} - \boldsymbol{I} \quad \rightarrow \quad \boldsymbol{E} = \frac{1}{2}(\boldsymbol{H} + \boldsymbol{H}^{\mathrm{T}} + \boldsymbol{H}^{\mathrm{T}} \cdot \boldsymbol{H}) \,. \tag{3}$$

If the deformation is sufficiently small, one might ignore higher-order terms (linearization) which leads to the *linear strain tensor*

$$\boldsymbol{\varepsilon} = \frac{1}{2}(\boldsymbol{H} + \boldsymbol{H}^{\mathrm{T}}) \,. \tag{4}$$

We describe the stress by the symmetric second-order *Cauchy stress tensor* $\boldsymbol{\sigma}$. The Cauchy stress maps a unit normal vector $\boldsymbol{n}$ onto a traction vector $\boldsymbol{t}$ in the current configuration by $\boldsymbol{t} = \boldsymbol{\sigma} \cdot \boldsymbol{n}$. For finite deformation settings it is useful to introduce a stress measure defined exclusively in the reference configuration and energy-conjugate to the Green-Lagrange strain tensor. Such a stress measure is given by the symmetric second Piola-Kirchhoff stress, which follows from the Cauchy stress tensor by a pull-back operation and by taking account of material volume changes:

$$\boldsymbol{S} = \det(\boldsymbol{F})\, \boldsymbol{F}^{-1} \cdot \boldsymbol{\sigma} \cdot \boldsymbol{F}^{-\mathrm{T}} \,. \tag{5}$$

The stiffness tensor describes the relation between changes of stress and changes of strain to first order, i. e. as a linear relationship

$$\mathrm{d}\boldsymbol{S} = \mathbb{C} : \mathrm{d}\boldsymbol{E} \,, \tag{6}$$

here given in a material setting. The stiffness tensor $\mathbb{C}$ and its inverse $\mathbb{C}^{-1}$, called compliance tensor, are fourth-order three-dimensional tensors. As we assume that the stress tensor is symmetric, i. e. limiting ourselves to non-polar materials, and as the strain tensors are symmetric, the stiffness tensor has the so-called *minor symmetries*:

$$C_{ijkl} = C_{jikl} \,, \quad C_{ijkl} = C_{ijlk} \,. \tag{7}$$

In our application examples, as we will describe in subsubsection 4.2.1, we assume the existence of a scalar potential, from which we obtain the *major symmetry*

$$C_{ijkl} = C_{klij} \,. \tag{8}$$

Therefore, $\mathbb{C}$ has only up to 21 instead of 81 independent components and can be mapped onto a symmetric second-order six-dimensional tensor using the Kelvin mapping (cf. e. g. Mehrabadi and Cowin, 1990; Nagel et al., 2016). This allows the generalization of different second-order tensor decompositions like the spectral or the polar decomposition to tensors of order four. In case of *isotropic elasticity*, the stiffness tensor takes the well-known coefficient form

$$C^{\mathrm{iso}}_{ijkl} = \lambda \delta_{ij}\delta_{kl} + \mu(\delta_{ik}\delta_{jl} + \delta_{il}\delta_{jk}) \quad \text{with} \quad \lambda = \frac{E\nu}{(1+\nu)(1-2\nu)} \quad , \quad \mu = \frac{E}{2(1+\nu)} \tag{9}$$

denoting Lamé's elastic constants, which can also be expressed using Young's modulus E and Poisson's ratio ν. The compliance tensor then follows as

$$C^{\mathrm{iso}\ -1}_{ijkl} = -\frac{\nu}{E}\delta_{ij}\delta_{kl} + \frac{1}{\mu}(\delta_{ik}\delta_{jl} + \delta_{il}\delta_{jk}) \,. \tag{10}$$

With this, a generalized representation of *Hooke's law* (cf. e. g. Nordmann et al., 2020) for isotropy can be expressed by

$$\boldsymbol{S} = \mathbb{C}_{\mathrm{iso}} : \boldsymbol{E} \quad \rightarrow \quad \boldsymbol{E} = \mathbb{C}^{-1}_{\mathrm{iso}} : \boldsymbol{S} \quad \text{and for small strains} \quad \boldsymbol{\sigma} = \mathbb{C}_{\mathrm{iso}} : \boldsymbol{\varepsilon} \quad \rightarrow \quad \boldsymbol{\varepsilon} = \mathbb{C}^{-1}_{\mathrm{iso}} : \boldsymbol{\sigma} \,. \tag{11}$$

There are different contractions of the stiffness and compliance tensor, which can be demonstrated easily assuming isotropic elasticity again. Providing any unit direction vector $\boldsymbol{d}$, the double contractions of the stiffness and compliance tensor with $\boldsymbol{d} \otimes \boldsymbol{d}$ is

equivalent to assuming a state of *uniaxial strain* and *uniaxial stress*, respectively. Another double contraction with $\boldsymbol{d} \otimes \boldsymbol{d}$ then results in a unidirectional measure of stiffness and compliance:

$$(\mathbb{C}_{\text{iso}} : \boldsymbol{d} \otimes \boldsymbol{d}) : \boldsymbol{d} \otimes \boldsymbol{d} = \; C^{\text{iso}}_{ijkl} \; d_i d_j d_k d_l = \lambda + 2\mu = \frac{E(1-\nu)}{(1+\nu)(1-2\nu)} =: P \,, \tag{12}$$

$$\left(\mathbb{C}^{-1}_{\text{iso}} : \boldsymbol{d} \otimes \boldsymbol{d}\right) : \boldsymbol{d} \otimes \boldsymbol{d} = {C^{\text{iso}}_{ijkl}}^{-1} \, d_i d_j d_k d_l = \frac{1}{E} \,. \tag{13}$$

It is important to note that these relations are not the inverse of each other. They are mechanically different assuming either a uniaxial strain or stress. Moreover, these measures have a precise physical interpretation: Taking the reciprocal of measure (13) returns a *Young modulus* whereas measure (12) represents the longitudinal wave modulus, i. e. *pressure wave modulus*, in the following just called p-wave modulus P. This can be verified considering another double contraction of the stiffness tensor obtained in elasto-dynamics. Starting from the local equilibrium of forces $\rho\ddot{\boldsymbol{u}} - \mathrm{Div}(\boldsymbol{\sigma}) = \boldsymbol{0}$, and inserting Hooke's law (11) as well as the plane wave solution $\boldsymbol{u} = \boldsymbol{m}\sin(\boldsymbol{d}\cdot\boldsymbol{x} - c\,t)$ with oscillation direction $\boldsymbol{m}$, placement $\boldsymbol{x}$, wave speed c, time t and density ρ yields the eigenvalue problem (a. k. a. Christoffel's equation)

$$\left(\boldsymbol{M} - \rho c^2 \boldsymbol{I}\right) \cdot \boldsymbol{m} = \boldsymbol{0} \quad \text{with} \quad \boldsymbol{M} = \boldsymbol{d} \cdot \mathbb{C}^{\mathrm{T}_{12}} \cdot \boldsymbol{d} \quad \text{and} \quad M_{ij} = C_{ijkl} d_j d_l \tag{14}$$

being the coefficients of the acoustic tensor. The formal 1−2 transposition of $\mathbb{C}$ can be omitted provided symmetry (7) holds. Obviously, the eigenvalues and eigenvectors of this tensor represent (scaled and squared) wave speeds and oscillation directions, respectively. For isotropic elasticity, the acoustic tensor reads

$$\boldsymbol{M} = \boldsymbol{d} \cdot \mathbb{C}_{\text{iso}} \cdot \boldsymbol{d} = \mu \boldsymbol{I} + (\lambda + \mu)\, \boldsymbol{d} \otimes \boldsymbol{d} \,. \tag{15}$$

From the singularity condition $\det(\boldsymbol{M} - M\boldsymbol{I}) = 0$ we then obtain the characteristic equation with the roots being the eigenvalues

$$M_1 = \lambda + 2\mu = P \quad , \quad M_2 = M_3 = \mu \quad \Leftrightarrow \quad c_1 = \sqrt{\frac{P}{\rho}} \quad , \quad c_2 = c_3 = \sqrt{\frac{\mu}{\rho}} \,. \tag{16}$$

Calculating the eigenvectors $\boldsymbol{m}$ it is found that the fast wave is a pure pressure wave (longitudinal polarization: $\boldsymbol{m} \cdot \boldsymbol{d} = 1$) and the other ones are pure shear waves (transverse polarization: $\boldsymbol{m} \cdot \boldsymbol{d} = 0$).

3 Glyph-Based Visualizations

As mentioned before, the visualization of tensors is, in most cases, highly dependent on the application. The same applies to the visualization of the stiffness tensor. Due to the special symmetries, certain analysis methods can be used, which allow different insights into the data.

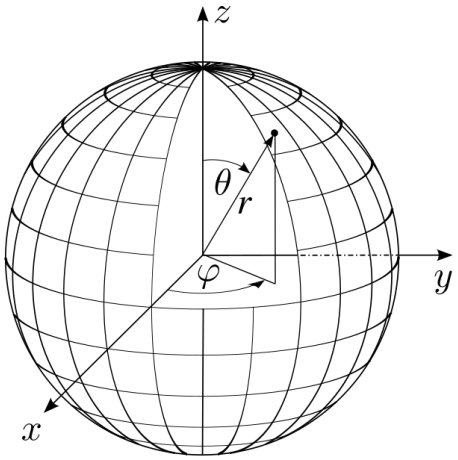

Fig. 1: Spherical coordinates

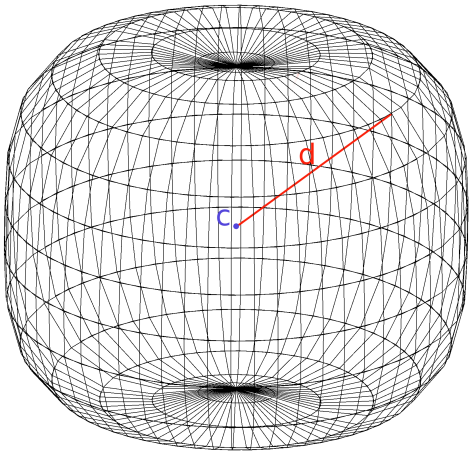

Fig. 2: Surface glyph design

There are several methods to design glyphs. Some are designed using geometric objects, and others by defining a distance function to a surface. In the following, these glyphs will be called *surface glyphs*. This type of glyph is described in Figure 2. The position $\boldsymbol{c}$ of the data in the global grid is the center of the glyph. The surface is then defined by vectors in each possible direction $\boldsymbol{d}$ emanating from $\boldsymbol{c}$. The length v of the vector $v\boldsymbol{d}$ is glyph-specific and specifies the distance of one surface point from the center. Further, we use a scale factor s with $v \rightarrow s \cdot v$ to scale the glyph. The factor s is chosen by the following guidelines:

1. no cluttering;
2. the shape of the glyph should be easy to recognize;
3. constant for a tensor field data set.

In order to be able to compare the glyphs, the scaling factor is given for each visualization. For the visualization, a finite number of points is generated on a grid with n_x points in the x direction and n_z points in the z direction using the following convention

$$\boldsymbol{d} = \begin{pmatrix} \sin(\theta)\ \cos(\varphi) \\ \sin(\theta)\ \sin(\varphi) \\ \cos(\theta) \end{pmatrix} \quad , \quad \begin{aligned} \theta &= \tfrac{\pi}{n_z} \cdot \alpha \\ \varphi &= \tfrac{2\pi}{n_x} \cdot \beta \end{aligned} \tag{17}$$

with $\alpha \in [0, n_z[$, $\beta \in [0, n_x[$. The surface grid points $\boldsymbol{g}$ corresponding to the direction $\boldsymbol{d}$ are then defined by

$$\boldsymbol{g} = \boldsymbol{c} + v\,\boldsymbol{d}. \tag{18}$$

3.1 Neeman Glyph

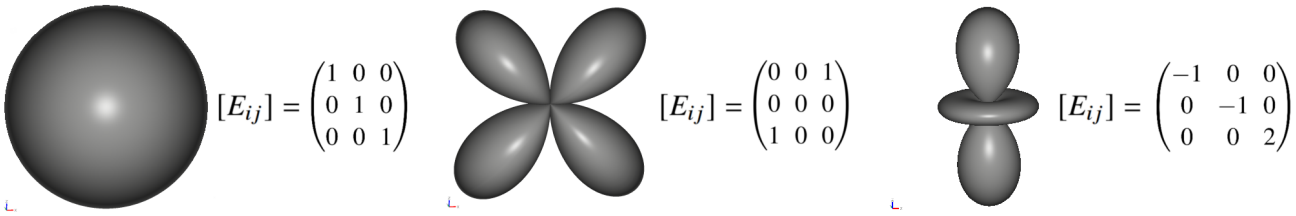

(a) Spherical tension (b) Pure shear (c) Triaxial tension

Fig. 3: Different deformation modes using the Reynolds glyph (cf. e. g. Kratz et al., 2013) without coloring the surface.

Neeman et al. (2008) used the Kelvin mapping in order to apply the polar decomposition on the stiffness tensor. On the resulting symmetric stretch part of the tensor they performed a spectral decomposition. This results in six eigenvalues and the corresponding six-dimensional eigenvectors. The inverse Kelvin mapping of the eigentensors produces six second-order three-dimensional tensors $\boldsymbol{E}$. These can be visualized using the Reynolds glyph. Therefore, a surface glyph as shown in Figure 2 is used, with the scalar

$$v = d_i E_{ij} d_j \quad \text{or} \quad v = \boldsymbol{E} : (\boldsymbol{d} \otimes \boldsymbol{d}) \tag{19}$$

as described in Equation 18. Thus, the scalars v simply represent the projection of the eigentensor onto the directions $\boldsymbol{d}$. The eigenvalues are represented by the color of the glyphs (though usually, the eigenvalues are used to *scale* the Reynolds glyphs). Some pure deformation modes visualized by the Neeman glyph are depicted in Figure 3. The eigentensor $\boldsymbol{E}$ corresponding to the *smallest* eigenvalue can be interpreted as a mode of strain corresponding to the lowest eigenstiffness. As this mode describes the most compliant one, it is used to visualize and analyze the potential of excessive deformation in some materials. In this work we will analyze the modes corresponding to *all six* eigenvalues.

3.2 Kriz Glyph

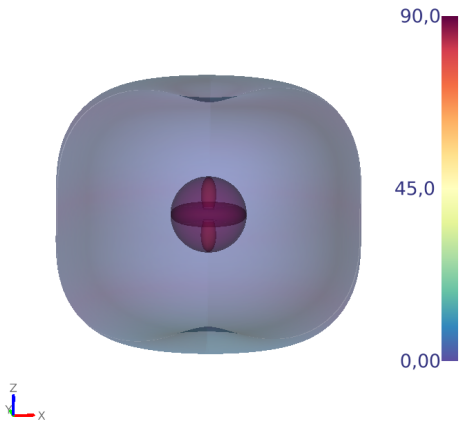

Fig. 4: Glyph design by Kriz et al. (2005) in a single view.

Kriz et al. (2005) used Christoffel's equation (14) to analyze the stiffness tensor with a special double contraction (cf. section 2). Thereby, the three-dimensional acoustic tensor $\boldsymbol{M}$ appears. Its eigenvalues and eigenvectors are functions of the stiffness tensor and some given wave propagation direction $\boldsymbol{d}$. To be precise, the three eigenvalues and eigenvectors describe the propagation speed c and oscillation direction $\boldsymbol{m}$ of plane waves, respectively, and can be calculated for any direction $\boldsymbol{d}$. The wave speeds corresponding to the three eigenvalues construct three different wave velocity surfaces, which describe the surfaces of three surface glyphs. Here, the wave speed c defines the scalar v described in Equation 18. The glyphs can be represented in one single view using transparent surfaces, see Figure 4, or in three different views. The color can be defined by the polarization (wave type), which is described by the angle between the vectors $\boldsymbol{m}$ and $\boldsymbol{d}$ ranging from 0° (longitudinal) to 90° (transverse).

Plane waves are waves where a given property only varies in the direction the wave travels, but is constant in the plane perpendicular to the direction of wave propagation (cf. section 2). Thus, the glyph describes how fast a wave of a certain type travels in a specific direction. The speed depends on the symmetry type and the stiffness of the material.

3.3 Hergl Glyph

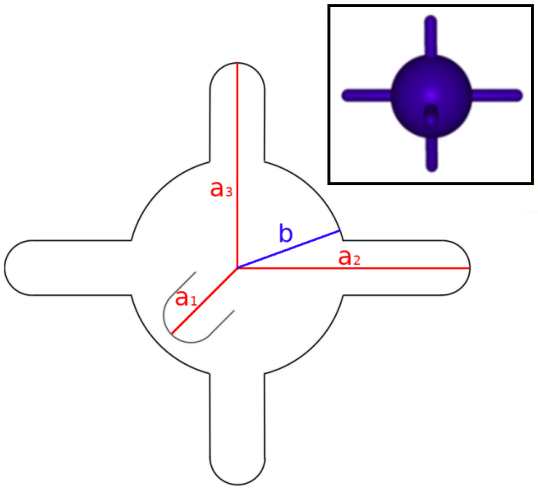

Fig. 5: Glyph design by Hergl et al. (2019) for an orthotropic stiffness tensor, where $a_\alpha \in \{P_\alpha, E_\alpha, P_\alpha^{-1}, E_\alpha^{-1}\}$.

Hergl et al. (2019) decomposed the stiffness tensor using the deviatoric decomposition

$$C_{ijkl} = C^{\text{iso}}_{ijkl} + \left(\delta_{ij} D_{kl} + \delta_{kl} D_{ij}\right) + \left(\delta_{ik}\hat{D}_{jl} + \delta_{il}\hat{D}_{jk} + \delta_{jk}\hat{D}_{il} + \delta_{jl}\hat{D}_{ik}\right) + D_{ijkl} \tag{20}$$

and the multipole representation (cf. e. g. Hergl et al., 2020). The multipoles enable the identification of the anisotropy type and the symmetries of the corresponding material. The color of the glyph reflects the anisotropy type. An example for a glyph representing an orthotropic stiffness tensor (three orthogonal symmetry planes) is given in Figure 5. Depending on this type, the symmetry plane normals of the material were calculated and represented by tubes with hemispheres on the ends: The number of the symmetry plane normals is denoted with n_n. Then, the length a_α of tube $\alpha \in [1, n_\text{n}]$ reflects the uniaxial stiffness measure $a_\alpha \in \{P_\alpha, E_\alpha\}$ in this direction $\boldsymbol{d}^\alpha$. According to the relations (12) and (13),

$$P_\alpha = \; C_{ijkl}\, d_i^\alpha d_j^\alpha d_k^\alpha d_l^\alpha \qquad \text{(uniaxial strain state)}\,, \tag{21}$$

$$E_\alpha = \left(C^{-1}_{ijkl}\, d_i^\alpha d_j^\alpha d_k^\alpha d_l^\alpha\right)^{-1} \qquad \text{(uniaxial stress state)}\,, \tag{22}$$

represent the p-wave modulus and Young's modulus for each direction $\boldsymbol{d}^\alpha$. A sphere in the center of the glyph represents the distance Δ to the isotropic tensor $\mathbb{C}^\text{iso}$ (9) as

$$\Delta = a_\text{min}\left(1 - \frac{\left\|\mathbb{C}^\text{ani}\right\|}{\left\|\mathbb{C}^\text{iso}\right\|}\right) \quad \text{with the anisotropic part} \quad \mathbb{C}^\text{ani} = \mathbb{C} - \mathbb{C}^\text{iso} \quad \text{and} \quad a_\text{min} = \min(a_\alpha)\,. \tag{23}$$

The glyph identifies the anisotropy type by color, thus allowing the differentiation of the tensor field into different regions with different anisotropy type. A closer look into single points provides information about the specific symmetries in the material, their orientation as well as their deviation from an isotropic material. Instead of the stiffness measures above, the glyph can also be used to highlight a compliance ($a_\alpha \in \{P_\alpha^{-1}, E_\alpha^{-1}\}$) in a given direction by using the inverse relations of (21) and (22), i. e.

$$P_\alpha^{-1} = \left(C_{ijkl}\, d_i^\alpha d_j^\alpha d_k^\alpha d_l^\alpha\right)^{-1}\,, \tag{24}$$

$$E_\alpha^{-1} = \; C^{-1}_{ijkl}\, d_i^\alpha d_j^\alpha d_k^\alpha d_l^\alpha\,. \tag{25}$$

As we will show in section 5, the visualization with the uniaxial stiffness measures (21)/(22) and the uniaxial compliance measures (24)/(25) can give different insights into the data.

3.4 Uniaxial Elasticity Glyph

A common method in crystallography and crystal plasticity is the visualization of the stiffness tensor using glyphs that represent a uniaxial elasticity measure in each direction. In the following this glyph will be called elasticity glyph. The uniaxial stiffness (or compliance) in a specified direction can be calculated by different procedures (cf. e.g. Böhlke and Brüggemann, 2001; Lago, 2017). As motivated in section 2 and specified in subsection 3.3 there are four such measures (21)/(22) and (24)/(25). They can be used as the scalar value v corresponding to each direction vector $\boldsymbol{d}$, defining the surface of the glyph as described in Figure 2. The surface color can optionally be used to point out the stiffness in this direction (cf. e.g. Böhlke and Brüggemann, 2001; Lago, 2017). This glyph describes obviously the directional stiffness/compliance at a given material point. It can thus also be used to determine the symmetry type and the symmetries of the material.

4 Examples

We use two different examples to compare the four explained glyph-based visualization methods. Both examples are physically non-linear and describe a deformation-induced anisotropy, but the application background is different. The first one represents a geometrically linear, one-dimensional problem (embedded in 2D), which was solved analytically. Thereby, small-strain ideal elasto-plasticity was applied, provoking a singular stiffness tensor under plastic flow. The second one is a geometrically non-linear, three-dimensional problem, which was solved numerically. Thereby, large-strain (hyper)elastic behavior was applied. Hence, the examples are chosen such that there is a simple (though not trivial) analytical one, and a more complex, fully non-linear numerical one. Having these very different features is beneficial to test and compare the visualization methods.

4.1 Small-strain von Mises plasticity – analytical solution

As a first example, an analytical, spherically symmetric problem representing an elasto-plastic thick-walled hollow sphere under pressure loading is analyzed. The example was taken from Nagel and Böttcher (2015), where the solution procedure is explained in detail. Pressure is exerted onto the inner surface of the hollow sphere such that the material partially plastifies during expansion of the sphere, i. e. that an inner shell deforms elasto-plastically while the outer shell remains elastic. Assuming monotonic loading, the radius of the elastic–plastic interface depends on the prescribed pressure. The resulting fields are expected to be of spherical symmetry as well. For visualization purposes, we analyze the intersection of the sphere with the global $y-z$ plane. Because of the constitutive formulation chosen (isotropic elasticity, von Mises plasticity), the plastic shell is expected to be in a homogeneous state (i. e. independent of the position within the shell) with a transversally isotropic symmetry distinguishing it from the still isotropically elastic outer shell. In this example, the stiffness tensor is elasto-plastic in the inner shell where the material has reached its elastic limit and flows plastically. Associated with the plastic flow is a decrease in overall stiffness (transition from elastic to elasto-plastic stiffness).

4.1.1 Derivation of the elasto-plastic stiffness tensor

Using spherical coordinates (radius $r \in [R_\mathrm{i}, R_\mathrm{a}]$, zenith/polar angle $\theta \in [0, \pi]$, azimuthal angle $\varphi \in [0, 2\pi]$)[1], the given boundary value problem (BVP)

$$u_{r,rr} + \frac{2}{r}u_{r,r} - \frac{2}{r^2}u_r = 0 \quad , \quad \sigma_{rr}(r = R_\mathrm{i}) = -p_\mathrm{i} \quad , \quad \sigma_{rr}(r = R_\mathrm{a}) = -p_\mathrm{a} \tag{26}$$

for the radial displacement field $u_r(r)$ can be solved analytically for linear *elastic* behavior. In order to solve the BVP for *elasto-plastic* behavior the following assumptions are made:

- spherical symmetry, no body forces acting,
- no pressure at the outer surface ($p_\mathrm{a} = 0$),
- von-Mises plasticity with associated flow rule and yield stress σ_F
- isotropic, linear elasticity with E and ν (or equivalently Lamé's constants λ, μ)

These conditions give rise to the following boundary value problem for the elasto-plastic shell

$$u_{r,r} + 2\frac{1}{r}u_r = \frac{(1-2\nu)\sigma_F}{E}\left[6\ln\frac{r}{r_p} + 2\left(\frac{r_p}{R_a}\right)^3\right]. \tag{27}$$

The solution of u_r must be continuous at the transition of the elastic and the elasto-plastic region. This condition defines the boundary value to solve this problem uniquely. The material parameters used in this work are given in Table 1:

Tab. 1: Material parameters for the elasto-plastic von Mises material model

E / Pa	ν	λ / Pa	μ / Pa	σ_F / Pa
$125 \cdot 10^9$	0.35	$\approx 108 \cdot 10^9$	$\approx 46.3 \cdot 10^9$	$300 \cdot 10^6$

In contrast to the purely elastic case, elasto-plastic behavior causes an internal interface w. r. t. the onset of plastic flow. The radial position r_p of this interface depends on the monotonically increasing load p_i and can be obtained solving a nonlinear equation. Assuming a given value $r_\mathrm{p} \in (R_\mathrm{i}, R_\mathrm{a})$, the solution for the radial displacement is given for two subdomains, i. e.

$$r \in [R_\mathrm{i}, r_\mathrm{p}] \text{ : elasto-plastic inner shell with} \qquad u_r = \frac{2\sigma_\mathrm{F}}{3E}r\left[\frac{3(1-\nu)}{2(1-2\nu)}\left(\frac{r_\mathrm{p}}{r}\right)^3 + \left(\frac{r_\mathrm{p}}{R_\mathrm{a}}\right)^3 + 3\ln\left(\frac{r}{r_\mathrm{p}}\right) - 1\right](1-2\nu), \tag{28}$$

$$r \in [r_\mathrm{p}, R_\mathrm{a}] \text{ : elastic outer shell with} \qquad u_r = \frac{2\sigma_\mathrm{F}}{3E}r\left[(1-2\nu)\left(\frac{r_\mathrm{p}}{R_\mathrm{a}}\right)^3 + \frac{1+\nu}{2}\left(\frac{r_\mathrm{p}}{r}\right)^3\right]. \tag{29}$$

[1] Note that in Nagel and Böttcher (2015) another convention was applied with θ being the azimuthal and φ being the polar angle. This results in a left-handed coordinate system. However, due to the spherical symmetry of the problem considered, there is no consequence of this.

The solution in the *elastic* subdomain is substituted into Hooke's law yielding the stresses for $[r_\mathrm{p}, R_\mathrm{a}]$:

$$\sigma_{rr}(r) = \frac{2}{3}\sigma_\mathrm{F}\left[\left(\frac{r_\mathrm{p}}{R_\mathrm{a}}\right)^3 - \left(\frac{r_\mathrm{p}}{r}\right)^3\right] \quad , \quad \sigma_{\theta\theta}(r) = \sigma_{\varphi\varphi}(r) = \frac{2}{3}\sigma_\mathrm{F}\left[\left(\frac{r_\mathrm{p}}{R_\mathrm{a}}\right)^3 + \frac{1}{2}\left(\frac{r_\mathrm{p}}{r}\right)^3\right] . \tag{30}$$

Then, the solution in the *elasto-plastic* subdomain is substituted into Hooke's law yielding the stresses for $[R_\mathrm{i}, r_\mathrm{p}]$:

$$\sigma_{rr}(r) = 2\sigma_\mathrm{F}\left(\ln\left(\frac{r}{r_\mathrm{p}}\right) + \frac{1}{3}\left[\left(\frac{r_\mathrm{p}}{R_\mathrm{a}}\right)^3 - 1\right]\right) \quad , \quad \sigma_{\theta\theta}(r) = \sigma_{\varphi\varphi}(r) = 2\sigma_\mathrm{F}\left(\ln\left(\frac{r}{r_\mathrm{p}}\right) + \frac{1}{3}\left[\left(\frac{r_\mathrm{p}}{R_\mathrm{a}}\right)^3 + \frac{1}{2}\right]\right) . \tag{31}$$

The stress tensor and its deviatoric part have thus the following coefficient matrices in orthonormal spherical coordinates:

$$[\sigma_{ij}] = \begin{pmatrix}\sigma_{rr} & 0 & 0\\ 0 & \sigma_{\theta\theta} & 0\\ 0 & 0 & \sigma_{\varphi\varphi}\end{pmatrix} \quad , \quad [\sigma_{ij}]^\mathrm{D} = \frac{1}{3}\begin{pmatrix}2\Delta\sigma & 0 & 0\\ 0 & -\Delta\sigma & 0\\ 0 & 0 & -\Delta\sigma\end{pmatrix} \tag{32}$$

$$\text{with } \Delta\sigma = \sigma_{rr} - \sigma_{\theta\theta} = \sigma_{rr} - \sigma_{\varphi\varphi} = \begin{cases} -\sigma_\mathrm{F} & : \ R_\mathrm{i} \le r \le r_\mathrm{p} \text{ (plastic)} \\ -\sigma_\mathrm{F}\left(\frac{r_\mathrm{p}}{r}\right)^3 & : \ r_\mathrm{p} \le r \le R_\mathrm{a} \text{ (elastic)} \end{cases} . \tag{33}$$

To proceed, the associated flow rule is considered with the plastic multiplier $\dot\Lambda$, the plastic potential g and the yield surface f:

$$\dot\varepsilon^\mathrm{p}_{ij} = \dot\Lambda\,\frac{\partial g}{\partial\sigma_{ij}} = \dot\Lambda g_{ij} \quad \text{with} \quad g \equiv f \quad \text{and} \quad f = \frac{1}{2}\sigma^\mathrm{D}_{ij}\sigma^\mathrm{D}_{ij} - \frac{1}{3}\sigma^2_\mathrm{F} . \tag{34}$$

Especially for this non-hardening von-Mises yield surface, we find $g_{ij} = f_{ij} = \sigma^\mathrm{D}_{ij}$. The deviatoric part of the stress tensor has the coefficient matrix

$$[\sigma_{ij}]^\mathrm{D} = \frac{\sigma_\mathrm{F}}{3}\Delta(r)\begin{pmatrix}-2 & 0 & 0\\ 0 & 1 & 0\\ 0 & 0 & 1\end{pmatrix} \qquad \text{with} \quad \Delta(r) = \begin{cases} 1 & : \ R_\mathrm{i} \le r \le r_\mathrm{p} \text{ (plastic)} \\ \left(\frac{r_\mathrm{p}}{r}\right)^3 & : \ r_\mathrm{p} \le r \le R_\mathrm{a} \text{ (elastic)} \end{cases} . \tag{35}$$

Thus, the functional dependence on the radial coordinate is moved to the function $\Delta(r)$, which is continuous, but not continuously differentiable. Introducing the second-order structural tensor $\boldsymbol{A}$, the deviatoric stress can be written in the tensorial form

$$\sigma^\mathrm{D}_{ij}\,\mathbf{e}_i\otimes\mathbf{e}_j = \frac{\sigma_\mathrm{F}}{3}\Delta(r)\left(\delta_{ij} - A_{ij}\right)\mathbf{e}_i\otimes\mathbf{e}_j \ \text{ with } \ \boldsymbol{A} = A_{ij}\,\mathbf{e}_i\otimes\mathbf{e}_j = 3\,\mathbf{e}_r\otimes\mathbf{e}_r . \tag{36}$$

The elasto-plastic tangent (stiffness tensor) reads (Scalet and Auricchio, 2018):

$$C^\mathrm{ep}_{ijkl} = C_{ijkl} - \frac{1}{d}\,C_{ijmn}g_{mn}\,f_{pq}C_{pqkl} \ \text{ with } \ d = f_{ij}C_{ijkl}g_{kl} . \tag{37}$$

Here, the isotropic fourth-order elasticity tensor with coefficients $C_{ijkl} = C^\mathrm{iso}_{ijkl}$ (9) is applied. In case of associated plasticity ($f_{ij} = g_{ij}$) the elasto-plastic tangent has major and minor symmetry. Else, the major symmetry is lost. Exploiting now $f_{ij} = g_{ij}$ and $f_{ii} = 0$ as well as $f_{ij} = f_{ji}$, the scalar d is calculated. First, the double contraction is obtained as

$$d_{kl} = f_{ij}C^\mathrm{iso}_{ijkl} = \lambda f_{ii}\delta_{kl} + \mu(f_{kl} + f_{lk}) = 2\mu f_{kl} = 2\mu\sigma^\mathrm{D}_{kl} \tag{38}$$

and with this it follows immediately

$$d = f_{ij}C^\mathrm{iso}_{ijkl}g_{kl} = d_{kl}g_{kl} = 2\mu f_{kl}f_{kl} = 2\mu\sigma^\mathrm{D}_{kl}\sigma^\mathrm{D}_{kl} = \frac{4}{3}\mu\sigma^2_\mathrm{F}\,\Delta^2(r) . \tag{39}$$

Exploiting the assured major symmetry $C^\mathrm{iso}_{ijkl} = C^\mathrm{iso}_{klij}$ of the elasticity tensor we further find

$$C^\mathrm{iso}_{ijmn}g_{mn}\,f_{pq}C^\mathrm{iso}_{pqkl} = f_{mn}C^\mathrm{iso}_{mnij}d_{kl} = d_{ij}d_{kl} = 4\mu^2\sigma^\mathrm{D}_{ij}\sigma^\mathrm{D}_{kl} = \frac{4}{9}\mu^2\sigma^2_\mathrm{F}\,\Delta^2(r)\left[\delta_{ij}\delta_{kl} - \delta_{ij}A_{kl} - A_{ij}\delta_{kl} + A_{ij}a_{kl}\right] . \tag{40}$$

Finally, the analytic expression for the elasto-plastic tangent modulus (the stiffness tensor) is

$$C^\mathrm{ep}_{ijkl} = C^\mathrm{iso}_{ijkl} - \frac{\frac{4}{9}\mu^2\sigma^2_\mathrm{F}\,\Delta^2(r)}{\frac{4}{3}\mu\,\sigma^2_\mathrm{F}\,\Delta^2(r)}\left[\delta_{ij}\delta_{kl} - \delta_{ij}A_{kl} - A_{ij}\delta_{kl} + A_{ij}A_{kl}\right] , \tag{41}$$

$$C^\mathrm{ep}_{ijkl} = (\lambda - \frac{1}{3}\mu)\delta_{ij}\delta_{kl} + \mu(\delta_{ik}\delta_{jl} + \delta_{il}\delta_{jk}) + \frac{1}{3}\mu\left(\delta_{ij}A_{kl} + A_{ij}\delta_{kl}\right) - \frac{1}{3}\mu A_{ij}A_{kl} = \text{const.} , \tag{42}$$

where it was used that the function $\Delta(r)$ is non-zero in the entire domain (hollow sphere). Thus, C^{ep}_{ijkl} does not explicitly depend on r. However, the anisotropy tensor $\boldsymbol{A}$ does depend on the (local) radial direction. The structure of the stiffness tensor can be captured very well using symbolic tensor notation:

$$\mathbb{C}_{\text{ep}} = \mu \left\{ \chi \boldsymbol{I} \otimes \boldsymbol{I} + 2\mathbb{S} + \frac{1}{3} \left(\boldsymbol{I} \otimes \boldsymbol{A} + \boldsymbol{A} \otimes \boldsymbol{I} - \boldsymbol{A} \otimes \boldsymbol{A} \right) \right\} \quad \text{with} \quad \chi = \frac{\lambda}{\mu} - \frac{1}{3} \quad \text{and} \quad S_{ijkl} = \frac{1}{2} \left(\delta_{ik}\delta_{jl} + \delta_{il}\delta_{jk} \right) . \tag{43}$$

The inverse of the stiffness tensor (the compliance tensor) defined by the requirement $\mathbb{C}_{\text{ep}} : \mathbb{C}^{-1}_{\text{ep}} = \mathbb{S}$ does not exist in this case due to the non-uniqueness of the elasto-plastic stress-strain relation. This is a consequence of the assumed *ideal* plastic behavior.[2] Mathematically speaking, the stiffness tensor is thus singular indicating a type of instability.
The presented analytical solution seems to be a suitable benchmark data set for visualizing stiffness tensors exhibiting transverse isotropy. Due to its simplicity it is easy to implement, and it still shows interesting features, such as (spherical) directionality in a field as well as discontinuity across an internal interface and singularity from a material instability.

4.1.2 Numerical calculation

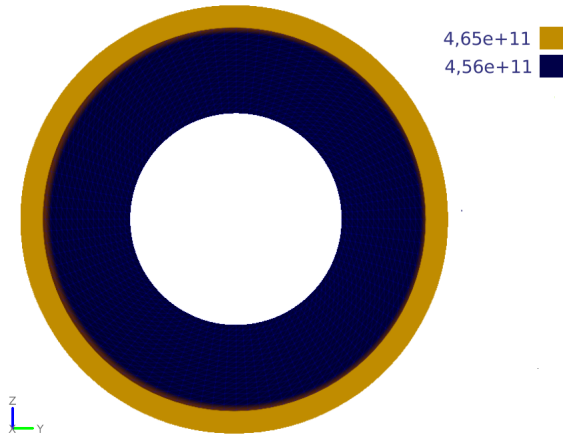

(a) Tensor norm (unit Pa) of the stiffness tensor for perfect precision (exact analytical values used): the tensor norm in the inner and outer shell is constant.

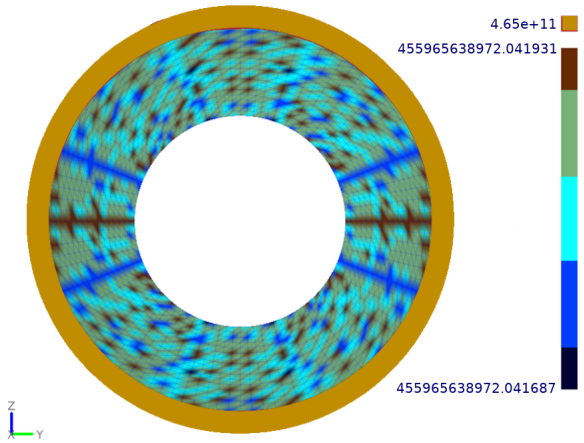

(b) Tensor norm of the stiffness tensor for double precision (15 significant digits of the floating point numbers): the tensor norm in the inner (elasto-plastic) shell has deviations beyond digit 15.

Fig. 6: Analytical Example: Tensor norm of the stiffness tensor.

The tensor norm of $\mathbb{C}_{\text{ep}}$ should be constant in the entire domain. However, there are perturbations due to limited double precision. This results from the numerical calculation of the anisotropic tensor components. Figure 6a depicts the *expected* norm and Figure 6b shows a detailed analysis of the *existing* norm. The norm of the stiffness tensor in the inner shell is around $4.56 \cdot 10^{11}$ Pa with the usual perturbations beyond digit 15. This very small inaccuracy results from the numerical calculation of the normalized vector $\boldsymbol{e}_r$. Let us consider the following example:

$$\boldsymbol{e}_r = \left(-6.84775296 \cdot 10^{-33}, \quad 0.587785065, \quad 0.809017131 \right)^{\text{T}} \quad \Rightarrow \quad |\boldsymbol{e}_r| = 1 + 8.88525386e^{-10} . \tag{44}$$

This error propagates to the resulting structural tensor $\boldsymbol{A}$ and further to the stiffness tensor $\mathbb{C}$. As described before, the analytical stiffness tensor $\mathbb{C}^{\text{ana}}$ in the elasto-plastic inner shell is singular. This becomes obvious using the Kelvin notation for $\mathbb{C}$ in the *local spherical* $\{r, \theta, \varphi\}$ coordinate system:

$$\left[C^{\text{ana}}_{ijkl} \right] = \begin{pmatrix} C_{rrrr} & C_{rr\theta\theta} & C_{rr\varphi\varphi} & \sqrt{2}\,C_{rr\theta\varphi} & \sqrt{2}\,C_{rrr\varphi} & \sqrt{2}\,C_{rrr\theta} \\ & C_{\theta\theta\theta\theta} & C_{\theta\theta\varphi\varphi} & \sqrt{2}\,C_{\theta\theta\theta\varphi} & \sqrt{2}\,C_{\theta\theta r\varphi} & \sqrt{2}\,C_{\theta\theta r\theta} \\ & & C_{\varphi\varphi\varphi\varphi} & \sqrt{2}\,C_{\varphi\varphi\theta\varphi} & \sqrt{2}\,C_{\varphi\varphi r\varphi} & \sqrt{2}\,C_{\varphi\varphi r\theta} \\ & & & 2\,C_{\theta\varphi\theta\varphi} & 2\,C_{\theta\varphi r\varphi} & 2\,C_{\theta\varphi r\theta} \\ & \text{sym} & & & 2\,C_{r\varphi r\varphi} & 2\,C_{r\varphi r\theta} \\ & & & & & 2\,C_{r\theta r\theta} \end{pmatrix} = \mu \begin{pmatrix} \chi+1 & \chi+1 & \chi+1 & 0 & 0 & 0 \\ \chi+1 & \chi+2 & \chi & 0 & 0 & 0 \\ \chi+1 & \chi & \chi+2 & 0 & 0 & 0 \\ 0 & 0 & 0 & 2 & 0 & 0 \\ 0 & 0 & 0 & 0 & 2 & 0 \\ 0 & 0 & 0 & 0 & 0 & 2 \end{pmatrix} . \tag{45}$$

Mathematically speaking, the stiffness tensor is thus ill-conditioned. Due to the numerical inaccuracies, the tensor becomes regular, but it is still close to singularity. For the numerical example (44) the tensor coefficients are given in Kelvin notation in the *global Cartesian* $\{x, y, z\}$ coordinate system:

$$\left[C^{\text{num}}_{ijkl} \right] = \begin{pmatrix} 185185185185.18518066 & 108587559359.75318909 & 122893922121.72825623 \\ 108587559359.75318909 & 200596753989.51571655 & 107482353317.39772034 \\ 122893922121.72825623 & 107482353317.39772034 & 186290391227.54064941 \\ 31134185674.891437531 & -1135583509.5823380947 & -29998602165.309085846 \\ -3.6271628009270536 91e-22 & 1.3229657927507670662e-23 & 3.4948662216519749713e-22 \\ -2.6352867451913345227e-22 & 9.611904425923671011e-24 & 2.5391677009320968429e-22 \end{pmatrix}$$

$$\begin{pmatrix} 31134185674.891437531 & -3.6271628009270536 91e-22 & -2.6352867451913345227e-22 \\ -1135583509.5823380947 & 1.3229657927507736784e-23 & 9.611904425923671011e-24 \\ -29998602165.30909729 & 3.4948662216519763819e-22 & 2.5391677009320968429e-22 \\ 29779521449.610321045 & 7.3177836555895179248e-22 & 5.3166784426726025652e-22 \\ 7.3177836555895179248e-22 & 9259259259 2.592590332 & -6.1939819056533223404e-54 \\ 5.3166784426726035056e-22 & -6.1939819056533234995e-54 & 9259259259 2.592590332 \end{pmatrix} .$$

[2] Of course, this can be prevented by introducing any kind of hardening during plastic flow.

From the mechanical point of view, the numerical inaccuracies might serve as a tiny amount of hardening, which is sufficient to make the stress-strain relation invertible and the stiffness tensor thus regular.

4.2 Indentation Test

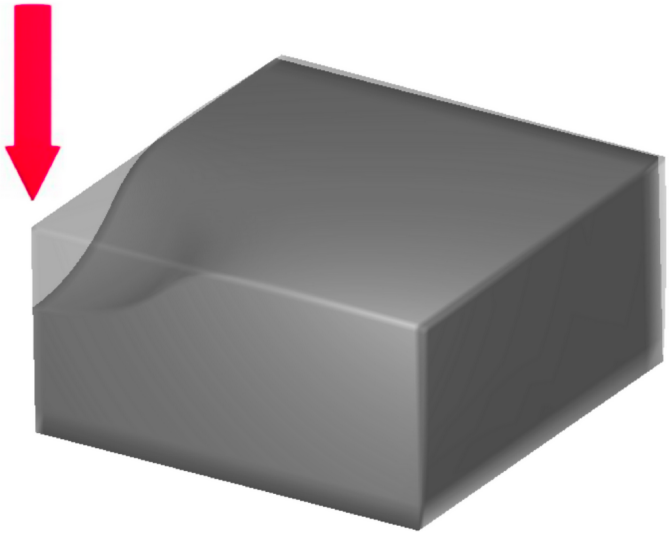

Fig. 7: Indentation test

As a second example, a simulation of an indentation test performed in FEBio (Ellis et al. (2012)) is chosen. Here, a spherical indenter was pressed into a soft biological material. The material is modelled as an initially isotropic, hyperelastic, strongly non-linear Ogden material Ogden (1972). One important consequence of this non-linearity is that anisotropic deformation will induce anisotropy in the material in a deformation-dependent manner. The data set contains 28 time steps with 9.375 data points on a regular grid. In this work, only the final time step (maximum indentation) is analyzed.

4.2.1 Hyperelastic materials

Hyperelastic formulations are a common choice in biomechanics (c. f. Grytz and Meschke, 2009; Federico and Gasser, 2010; Görke et al., 2010; Moerman et al., 2016, and references therein). Here, in a purely mechanical setting, we introduce the free Helmholtz energy density (strain energy density) $\psi = \psi(\boldsymbol{E})$ as a potential from which the second Piola-Kirchhoff stress tensor can be derived as energy-conjugate to the Green-Lagrange strain:

$$\boldsymbol{S} = \frac{\partial \psi}{\partial \boldsymbol{E}} = 2\frac{\partial \psi}{\partial \boldsymbol{C}} \,. \tag{46}$$

Further, the stiffness tensor can be calculated by

$$\mathbb{C} = \frac{\partial \mathbf{S}}{\partial \boldsymbol{E}} = 4\frac{\partial^2 \psi}{\partial \boldsymbol{C}^2} \,. \tag{47}$$

In isotropic hyperelasticity, $\psi(\boldsymbol{C})$ can be expressed in terms of the eigenvalues of $\boldsymbol{C}$ or their square roots, i. e. the principal stretches: $\psi(\lambda_1, \lambda_2, \lambda_3)$. With

$$\boldsymbol{C} = \sum_{i=1}^{3} \lambda_{(i)}^2 \boldsymbol{N}_{(i)} \otimes \boldsymbol{N}_{(i)} \,, \tag{48}$$

where the brackets around the indices indicate that no summation convention is used, we find by virtue of the chain rule

$$\boldsymbol{S} = 2\frac{\partial \psi}{\partial \boldsymbol{C}} = \sum_{i=1}^{3} \frac{1}{\lambda_{(i)}} \frac{\partial \psi}{\partial \lambda_{(i)}} \boldsymbol{N}_{(i)} \otimes \boldsymbol{N}_{(i)} = \sum_{i=1}^{3} S_{(i)} \boldsymbol{N}_{(i)} \otimes \boldsymbol{N}_{(i)} \,. \tag{49}$$

The stiffness tensor then follows as

$$\mathbb{C} = \sum_{i,j=1}^{3} \frac{1}{\lambda_{(j)}} \frac{\partial S_{(i)}}{\partial \lambda_{(j)}} \boldsymbol{N}_{(i)} \otimes \boldsymbol{N}_{(i)} \otimes \boldsymbol{N}_{(j)} \otimes \boldsymbol{N}_{(j)} + \sum_{i,j=1;\, i \neq j}^{3} \frac{S_{(j)} - S_{(i)}}{\lambda_{(j)}^2 - \lambda_{(i)}^2} \Big(\boldsymbol{N}_{(i)} \otimes \boldsymbol{N}_{(j)} \otimes \boldsymbol{N}_{(i)} \otimes \boldsymbol{N}_{(j)} + \boldsymbol{N}_{(i)} \otimes \boldsymbol{N}_{(j)} \otimes \boldsymbol{N}_{(j)} \otimes \boldsymbol{N}_{(i)} \Big). \tag{50}$$

The occurrence of deformation-induced anisotropy can be anticipated from the dependence of the stiffness tensor on the principal stretch values λ and directions $\boldsymbol{N}$.

One example for this material class, typically used for biological materials, is the family of Ogden models described by Ogden (1972) and given by the strain energy density formulation

$$\psi = \sum_{i=1}^{n} \frac{\mu_i}{m_i} \left(\lambda_1^{m_i} + \lambda_2^{m_i} + \lambda_3^{m_i} - 3 \right). \tag{51}$$

In the sequel, we have used the following variant of the Ogden model implemented into the open-source finite element software FEBio (Ellis et al., 2012)

$$\psi = \frac{1}{2} c_p (J-1)^2 + \frac{c_1}{m_1^2} \left(\lambda_1^{m_1} + \lambda_2^{m_1} + \lambda_3^{m_1} - 3 - m_1 \ln J \right) \tag{52}$$

where $J = \det \boldsymbol{F} = \lambda_1 \lambda_2 \lambda_3$ and c_p, c_1, m_1 are material parameters.

5 Results

We used the analytical example described in subsection 4.1 and the indentation test described in subsection 4.2 to compare the different glyph types.

5.1 Analytical Example

The different glyph visualizations for the elasto-plastic example are presented in the following paragraphs. We selected 44 data points of the tensor field. These data points are chosen such that they cover the entire field and are distributed symmetrically.

5.1.1 Neeman Glyph

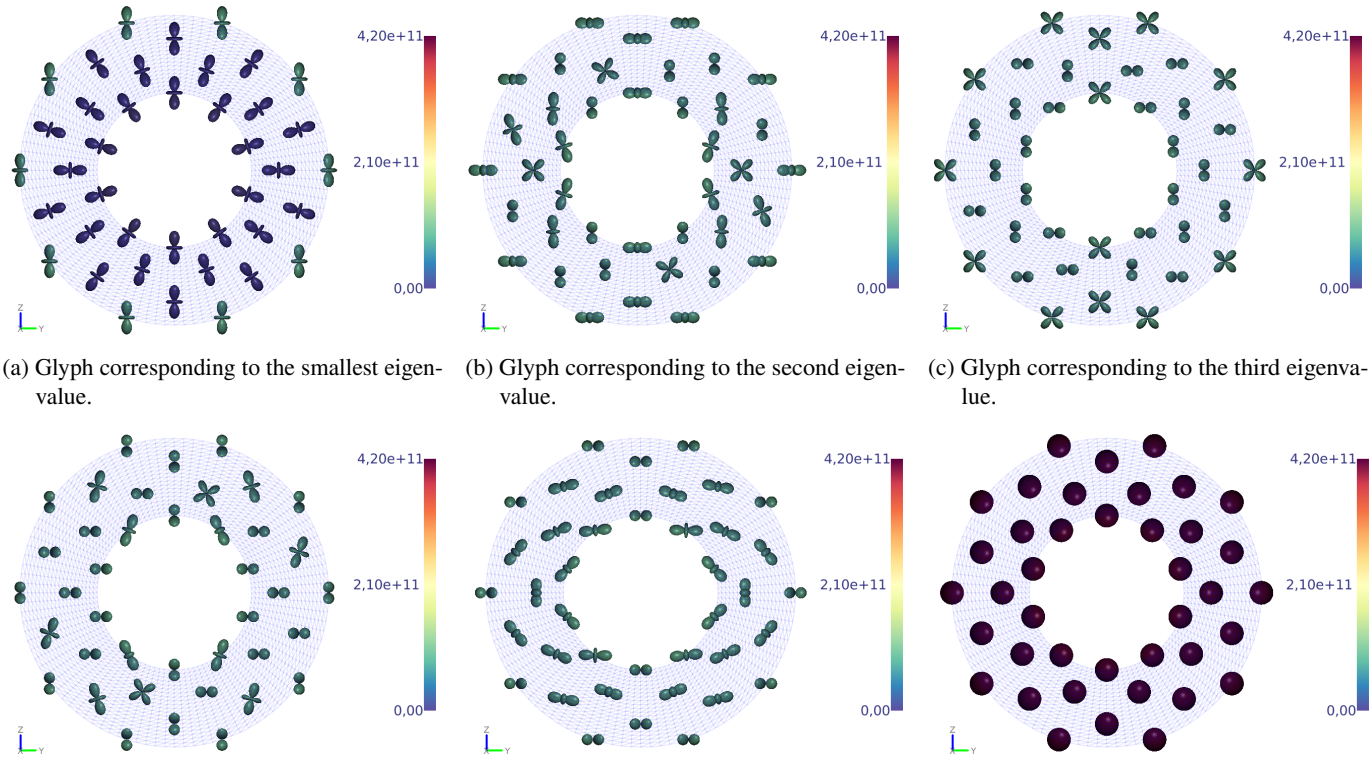

(a) Glyph corresponding to the smallest eigenvalue.

(b) Glyph corresponding to the second eigenvalue.

(c) Glyph corresponding to the third eigenvalue.

(d) Glyph corresponding to the fourth eigenvalue.

(e) Glyph corresponding to the fifth eigenvalue.

(f) Glyph corresponding to the largest eigenvalue.

Fig. 8: Analytical example: Glyph designed by Neeman et al. (2008). The color legend is given in Pa.

The results of the visualization of the elasto-plastic example using the glyph presented by Neeman et al. (2008) is shown in Figure 8. As explained before, the glyph described by Neeman et al. analyzed the modes associated with the *smallest* eigenvalue of the stretch part of the stiffness tensor. Figure 8 displays *all six* modes. Figure 8a starts with the mode associated with the lowest eigenstiffness. The high values in the outer shell show that the material behaves very stiff in the elastic range. Compared to that, the eigenstiffness in the inner (elasto-plastic) shell is almost zero. From the mechanical point of view it should be exactly zero, indicating no resistance of plastic flow in radial direction. However, due to the numerical inaccuracies (cf. subsubsection 4.1.2) this eigenvalue is not 0 but 36.9 Pa. The corresponding glyphs shown in Figure 8a represent triaxial compression (cf. also Figure 3). The glyphs in the inner shell are oriented radially, which is a result of the spherically symmetric plastic flow. The glyphs in the outer shell are parallel to the global z direction. This is an artifact, because isotropic tensors do not contain directional information.

In this case, the glyph is oriented by the global coordinate system, which however can be misleading. Figure 8f displays the glyphs corresponding to the largest eigenvalue representing all spherical tension. The largest eigenstiffness corresponds to a hydrostatic eigendeformation associated with the bulk modulus of the material. The scale of the glyphs in the inner and the outer shell is identical since the bulk stiffness does not change by the von-Mises plastic flow.
In Figure 8b – Figure 8e, the glyphs in the inner shell represent pure shear or triaxial tension. Their non-uniform orientation can be explained by the fact that the corresponding eigenvalues are multiple eigenvalues. Thus, the figures corresponding to the multiple eigenvalues must be analyzed in combination. Additionally, it must be noted that the eigentensors corresponding to multiple eigenvalues must be interpreted as eigenspace. The symmetries of the tensor field are given by this eigenspace, not the single eigentensors. A figure with all four glyphs in a single view can be found in the appendix in Figure 16. In this numerical example there is one double eigenvalue and two others that are similar to this double eigenvalue. It follows that the glyphs corresponding to these four eigenvalues cannot be sorted into unique fields. In Figure 8b – Figure 8e, the glyphs in the outer shell represent pure shear. For the same reason as for Figure 8a, the glyphs are oriented according to the global coordinate system.

5.1.2 Kriz Glyph

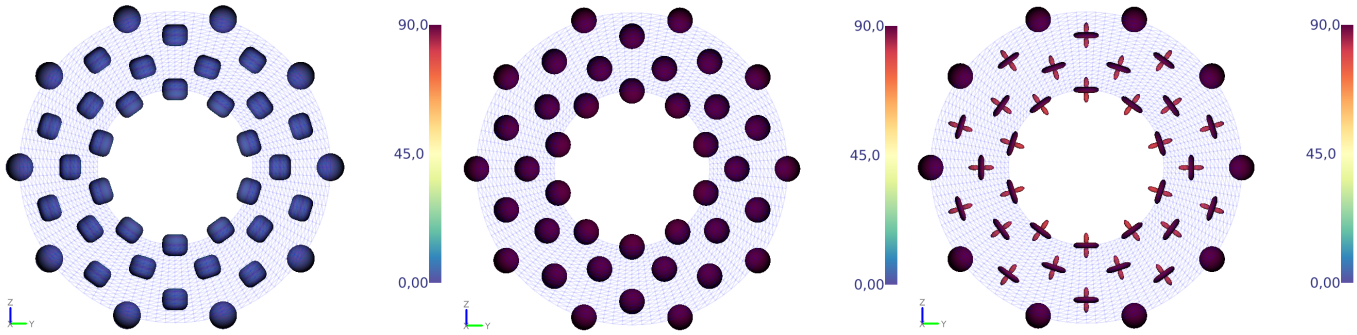

(a) Fast wave, scaled by the factor 10^{-13}. (b) Intermediate wave, scaled by the factor $4 \cdot 10^{-13}$. (c) Slow wave, scaled by the factor $4 \cdot 10^{-13}$.

Fig. 9: Analytical Example: Glyph designed by Kriz et al. (2005) representing the plane waves. The color depicts the polarization angle in °. More detailed pictures can be found in the appendix in Figure 17-Figure 19.

The glyph visualization by Kriz et al. (2005) representing the plane waves results in three different glyphs. The three independent plane waves are classified with respect to their speed. Hence, there is a *fast*, an *intermediate* and a *slow* wave.[3] These glyphs can be displayed in a single view or in multiple ones. For a better overview, we use three views. The first one, displayed in Figure 9a, describes the fast wave, which can be recognized by the scale of the glyphs. The intermediate and slow waves are displayed in Figure 9b and Figure 9c. In general, the waves have a mixed mode, i. e. wave propagation and oscillation direction are neither parallel nor perpendicular to each other (cf. subsection 3.2). Only for isotropy, the fast wave is a pure longitudinal wave (primary/pressure wave), and intermediate and slow wave are pure transverse waves with the same speed (secondary/shear wave). In this isotropic case, the Kriz glyphs are spherical. This can be observed in the outer shell of the domain: The radius and the type of the slow and intermediate waves are identical. Thus, there are only two independent waves in the isotropic outer shell. In the inner shell, there are three different waves. The fast wave is nearly longitudinal (0°), the intermediate wave is nearly transverse (90°) and the slow wave has different polarizations in different directions. Further, we clearly see that the intermediate wave is isotropic. Mechanically speaking, this is the transverse wave oscillating in the plane of isotropy (shear in the $\theta - \varphi$ plane). The slow wave is of mixed type and the glyph deviates from the spherical shape due to the strong anisotropy transversal to the $\theta - \varphi$ plane. Thus, there are three independent glyphs indicating three independent waves. These three glyphs are symmetric by a rotation around the radial axis. The anisotropy type and alignment, which corresponds to the transverse isotropy, can thus be determined from the three representations. The single symmetry plane normal corresponds to the radial axis (cf. appendix Figure 17-Figure 19).
Finally, we note that these waves are unlikely to occur in reality since they are obtained from the elasto-*plastic* stiffness tensor. Hence, the excitation would require to reach the yield limit, but plastic dissipation would then stop wave propagation very soon. Moreover, these waves must be considered here as a tool to visualize the underlying anisotropy.

5.1.3 Hergl Glyph

The glyph described by Hergl et al. (2019) focuses on the symmetries of the material. These can be determined from Figure 10. The material is transversally isotropic in the inner shell and isotropic in the outer shell. Figure 10a and Figure 10c display the two uniaxial stiffness measures of the material, Figure 10b and Figure 10d display the two uniaxial compliance measures. Figure 10a and Figure 10b use the stiffness tensor for the calculations, and Figure 10c and Figure 10d use the compliance tensor (cf. subsection 3.3).
As mentioned before, the compliance tensor only exists because of the limited precision (floating point errors) in the stiffness tensor data. Thus, the glyphs in Figure 10c and Figure 10d should not exist in theory. In practice, they do exist and can be interpreted to some extent. However, the scale of the glyphs is affected noticeably by the near singularity of the stiffness tensor.

[3] Kriz et al. (2005) used a similar, but somewhat more abstract terminology of *major, intermediate, minor* wave.

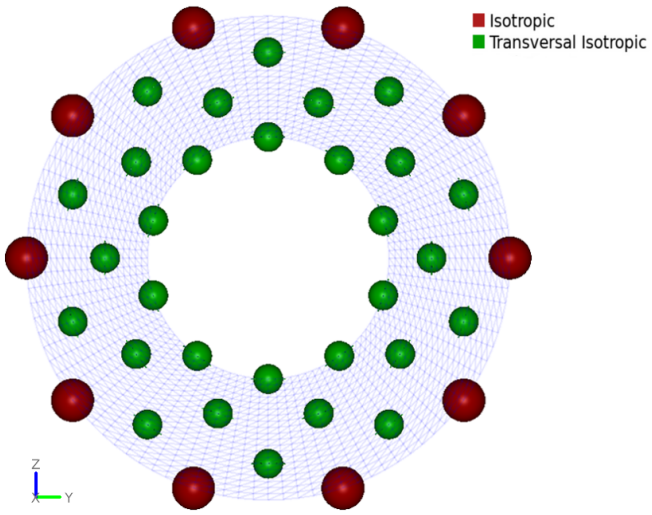

(a) Stiffness P($\mathbb{C}$): Scaled by the factor 10^{-13}.

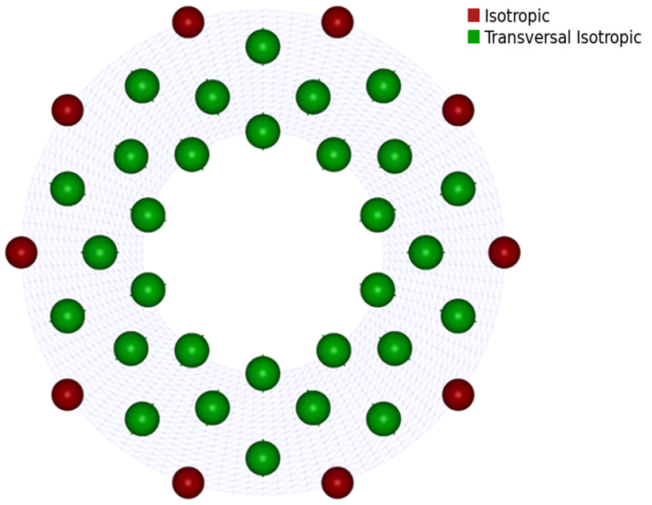

(b) Compliance $\mathrm{P}^{-1}(\mathbb{C})$: Scaled by the factor $3 \cdot 10^{9}$.

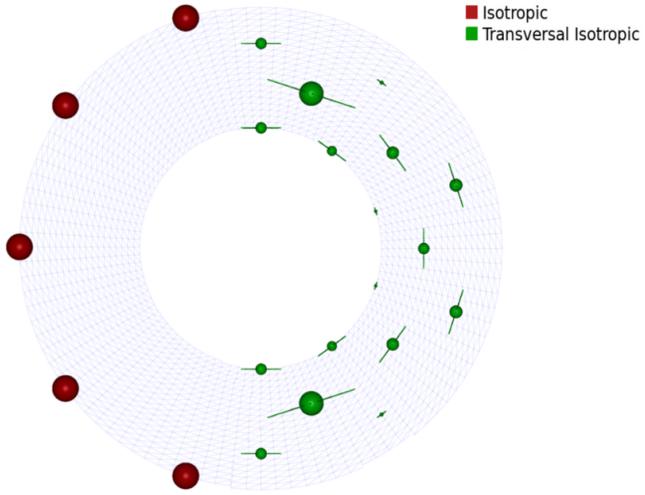

(c) Stiffness $\mathrm{E}(\mathbb{C}^{-1})$: Left: outer shell, scaled by the factor 10^{-13}; Right: inner shell, scaled by the factor 100.

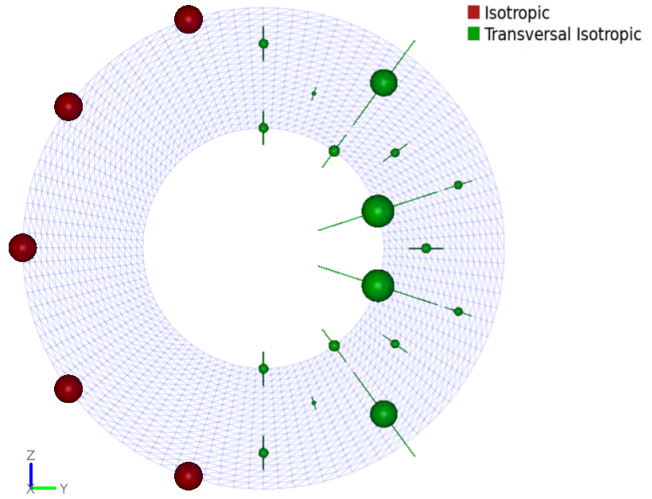

(d) Compliance $\mathrm{E}^{-1}(\mathbb{C}^{-1})$: Left: outer shell, scaled by the factor 1; Right: inner shell, scaled by the factor 10^{-6}.

Fig. 10: Analytical Example: Glyph designed by Hergl et al. (2019) visualizing the symmetries of the material. The length of the tubes either represents a stiffness (P: p-wave modulus, E: Young's modulus) or the corresponding compliance.

Analyzing the orientation of all the glyphs in more detail shows that the single symmetry plane normal is oriented radially. The distance to the isotropic case, defined by Eq. (23), seems to be bigger in the glyphs based on the compliance tensor. This results from the fact that the size of the sphere is calculated using the smallest value for the stiffness/compliance, which can be misleading. The glyph based on the stiffness tensor, depicted in Figure 10a, shows that the material has a larger p-wave modulus in the outer shell than in the inner one. The same tendency can be seen in Figure 10c, where Young's modulus calculated from the compliance tensor is depicted. In this case the differences of the stiffness are much more highlighted than in Figure 10a. The glyphs in Figure 10c in the outer shell are scaled by the factor 10^{-13} and in the inner shell by the factor 100. From this it follows that the material in the outer shell is much stiffer than in the inner shell due to the expected softening in the region of plastic flow. In the inner shell the material is less stiff in radial direction than perpendicular to it. The glyphs displaying the compliance, displayed in Figure 10b and Figure 10d, show the inverse glyph and therefore the same behaviour.

5.1.4 Uniaxial Elasticity Glyph

The glyphs visualizing the uniaxial elasticity (cf. e. g. Böhlke and Brüggemann, 2001; Lago, 2017) are shown in Figure 11. Figure 11a and Figure 11c display the two uniaxial stiffness measures of the material, Figure 11b and Figure 11d display the two uniaxial compliance measures. As described in the previous paragraph, the glyphs using the compliance tensor for the calculations should not exist. It can be seen clearly in Figure 11c that there are severe problems for the Young modulus E calculated from the compliance tensor. This occurs when the scalar on the right hand side of Eq. (22) is nearly zero in some directions and the reciprocal value thus gets extremely large. Further, it can be recognized that the size of the glyphs displayed in Figure 11d varies. Again, this comes from the near singularity of the stiffness tensor and the limited precision of its coefficients. In the three cases (a, b, d) where a glyph exists, the glyphs of the inner shell are oriented in radial direction. Each of the glyphs is symmetric to a rotation around this axis. This implies transversal isotropy of the material. The glyphs in the outer shell are spheres, which means that the material is isotropic in this area. The glyphs in the outer shell displayed in Figure 11a are bigger than these in the inner

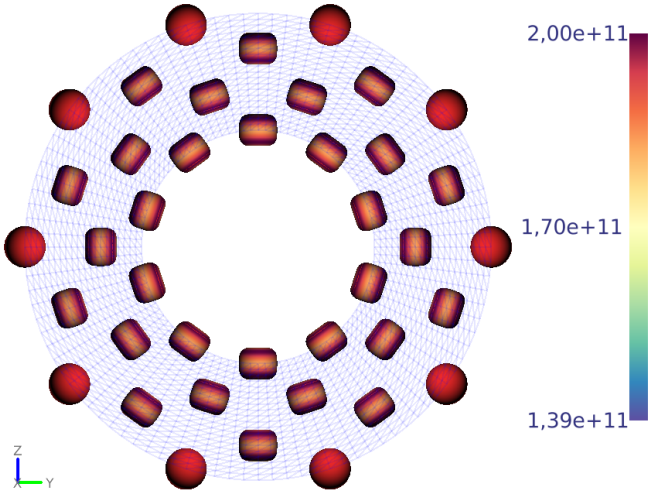

(a) Stiffness $\mathrm{P}(\mathbb{C})$: Scaled by the factor 10^{-13}.

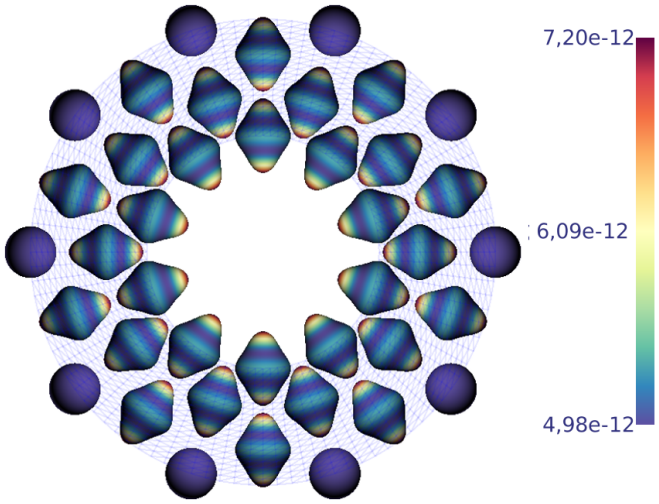

(b) Compliance $\mathrm{P}^{-1}(\mathbb{C})$: Scaled by the factor $5 \cdot 10^{9}$.

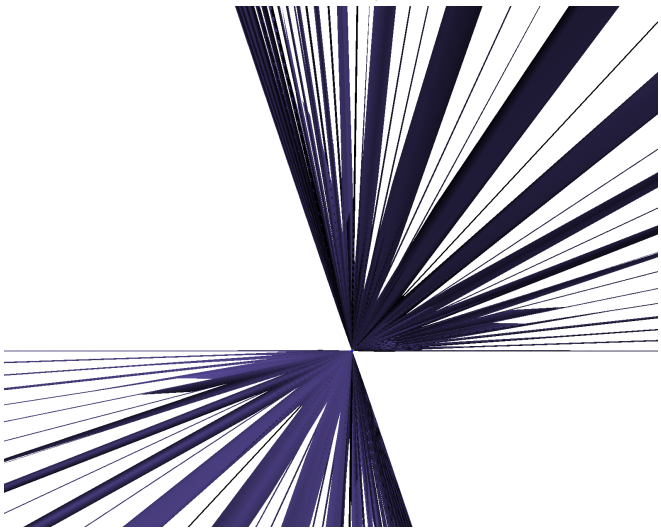

(c) Stiffness $\mathrm{E}(\mathbb{C}^{-1})$: Scaling irrelevant.

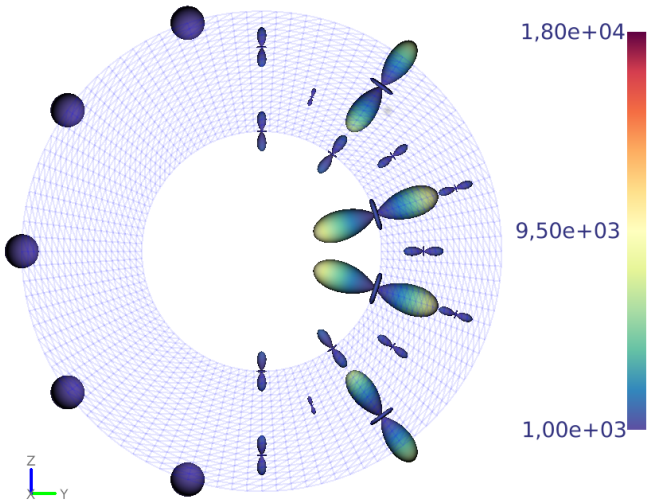

(d) Compliance $\mathrm{E}^{-1}(\mathbb{C}^{-1})$: Left: outer shell, scaled by the factor 1; Right: inner shell, scaled by the factor 10^{-6}.

Fig. 11: Analytical example: Glyph visualizing the uniaxial elasticity (stiffness/compliance) of the material, described by Böhlke and Brüggemann (2001) or Lago (2017). The color legend is given in Pa for the glyphs describing the stiffness and in Pa^{-1} for the glyphs describing the compliance.

shell, but the differences are not pronounced. Figure 11b displays the compliance measures based on the compliance tensor and shows the inverse glyph and thus the same behaviour. Still, the convex shape of the glyphs allows a better visualization of the anisotropic properties in this case.

5.2 Indentation Test

We selected 39 data points of the tensor field. These data points are chosen such that they cover the entire field. The distance between the data points in the indentation area is smaller than the distance of the glyphs in the rest of the field. The reason is that the material undergoes much larger deformations in the area of indentation than in the rest of the domain. An exception is made by the presentation of the third glyph. This glyph is designed to picture many data points. Thus, for this method all data points are visualized.

5.2.1 Neeman Glyph

The visualization of the indentation test using the glyph presented by Neeman et al. (2008) is illustrated in Figure 12. The smallest eigenvalue of the stretch part, visualized by the color of the glyph in Figure 12a, lies in the value range from around 0.0008 to 0.0037 MPa. This implies that the described material is a soft material. The closer the material point is to the center of the indentation, the stiffer the material gets, which is in line with its non-linear behavior. The glyphs in the regions of larger deformation show that the most compliant mode is pure shear. In the rest of the domain the most compliant mode varies between triaxial compression and pure shear. This can be explained by the fact that the eigenvalues of the stretch part of the stiffness tensor are similar. The eigenvalues are displayed in the appendix in Figure 21.
As recalled in subsubsection 4.2.1, the eigenvectors of the Cauchy-Green tensor equal the principal stretch directions and the

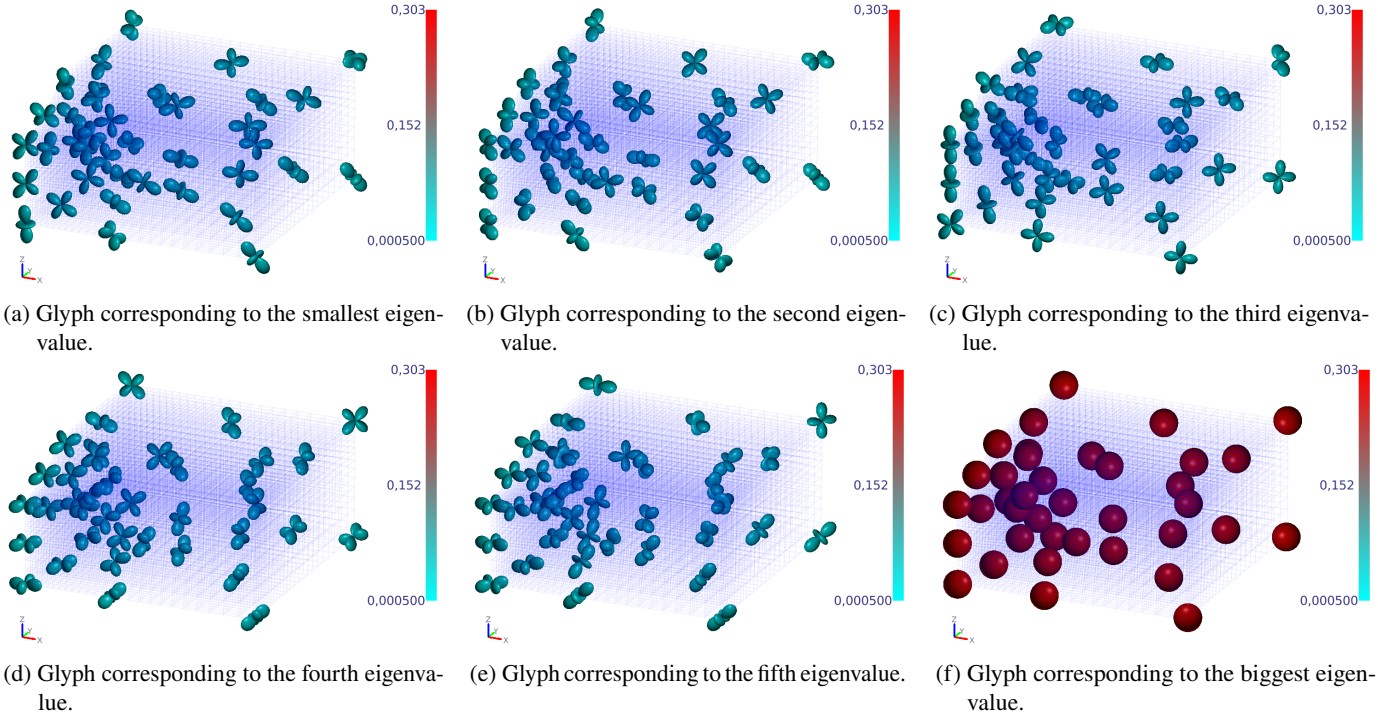

(a) Glyph corresponding to the smallest eigenvalue.
(b) Glyph corresponding to the second eigenvalue.
(c) Glyph corresponding to the third eigenvalue.
(d) Glyph corresponding to the fourth eigenvalue.
(e) Glyph corresponding to the fifth eigenvalue.
(f) Glyph corresponding to the biggest eigenvalue.

Fig. 12: Glyph designed by Neeman et al. (2008). The unit of the color bar is given in MPa.

Ogden-type material model is based on them. Consequently, the main direction of the glyphs representing triaxial compression modes is aligned with the dominant principal stretch direction. The glyphs representing pure shear are aligned in the plane where the largest deformations occur. The bisecting lines of the glyph's main axes equal the dominant principal stretch directions.
The glyphs corresponding to the eigenvalues depicted in Figure 12b – Figure 12e represent triaxial compression and shear. They are all oriented similar to the glyphs described before. The glyphs displayed in Figure 12f are all nearly identical. They represent the eigentensor corresponding to the biggest eigenvalue and describe spherical tension. This is a consequence of the near-incompressibility observed in many biological tissues.

5.2.2 Kriz Glyph

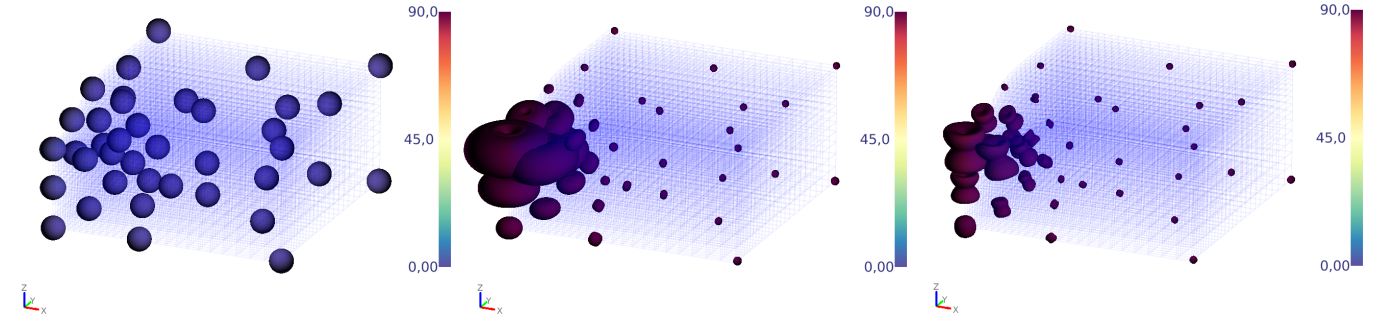

(a) Fast wave: Scaled by the factor 500.
(b) Intermediate wave: Scaled by the factor $3 \cdot 10^4$.
(c) Slow wave: Scaled by the factor $3 \cdot 10^4$.

Fig. 13: Indentation test: Plane wave glyph designed by Kriz et al. (2005), see also Figure 20 in the appendix. The color depicts the polarization angle in °.

In contrast to the fast wave glyphs in Figure 13a, the intermediate and slower waves in Figure 13b and Figure 13c are scaled by the factor 60 higher. They have a transverse or nearly transverse character and can be considered as shear waves, consequently. Obviously, the shear wave velocities in the region around the compressed material are significantly higher than in the rest of the material because of the deformation-dependent stiffening of this shear-dominated material. The fast waves are all longitudinal or, in the strongly compressed region, nearly longitudinal, which can be recognized by the color of the glyphs in Figure 13a. Once again this is a consequence of the high volumetric stiffness of the material. It can also be recognized that the material in the less deformed region of the tissue is nearly isotropic, because the glyphs of all three waves are nearly spherical. The closer the glyph is to the center of the indentation zone, the more the shear wave velocities become direction-dependent. The fast wave glyphs in this zone change their shape only slightly, which means their direction-dependence is not as strong. The combination of the shape of the three glyphs shows that the material close to the center of the indentation is transversally isotropic or nearly transversally isotropic. The axes of symmetry equal the dominant principal stretch directions.

5.2.3 Hergl Glyph

The glyph presented by Hergl et al. (2019) focuses on the symmetries of the material. It can be seen in Figure 14 that the material is transversally isotropic near the indentation center and orthotropic in the rest of the material. The degree of orthotropy, described by the distance of the sphere's radius and the smallest normal, is low. In effect, the material is nearly isotropic because of the small deformations in this region. Near the transversally isotropic region the glyphs differ strongly from a sphere, which means that the tensor differs much more from an isotropic tensor than in the (almost) undeformed regions. This is due to the deformation-induced stiffening of the material.

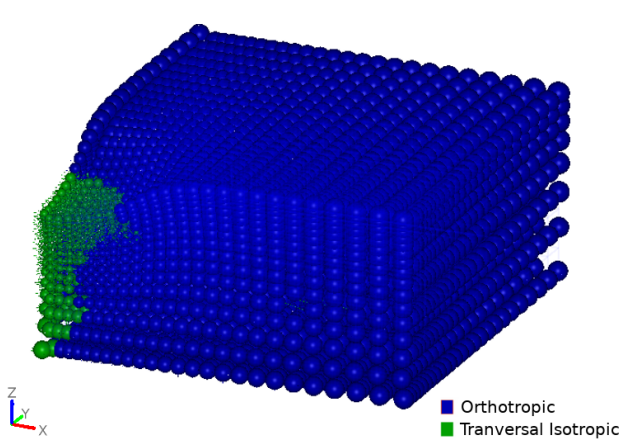

(a) Stiffness $\mathrm{P}(\mathbb{C})$: Scaled by the factor 300.

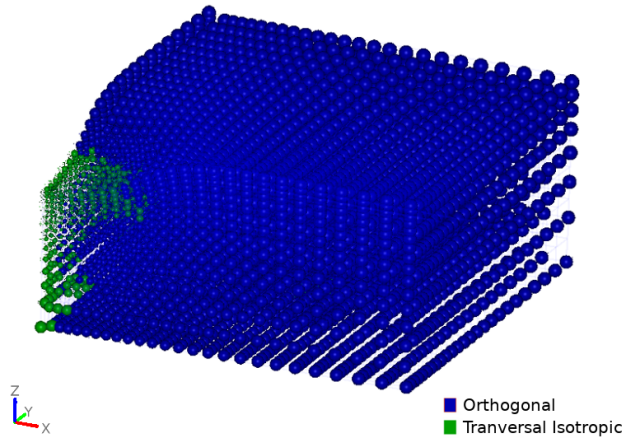

(b) Compliance $\mathrm{P}^{-1}(\mathbb{C})$: Scaled by the factor 2.

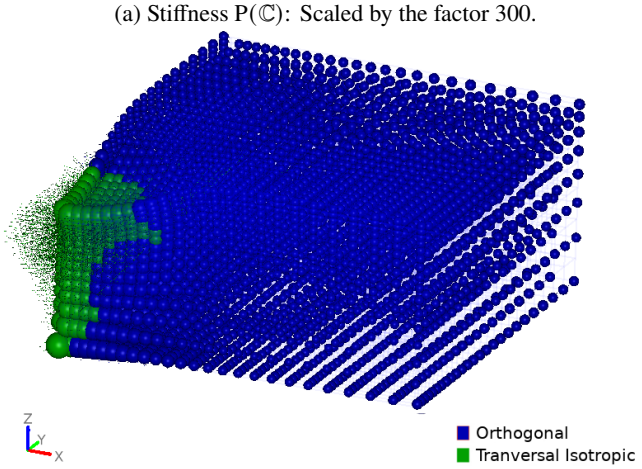

(c) Stiffness $\mathrm{E}(\mathbb{C}^{-1})$: Scaled by the factor 10000.

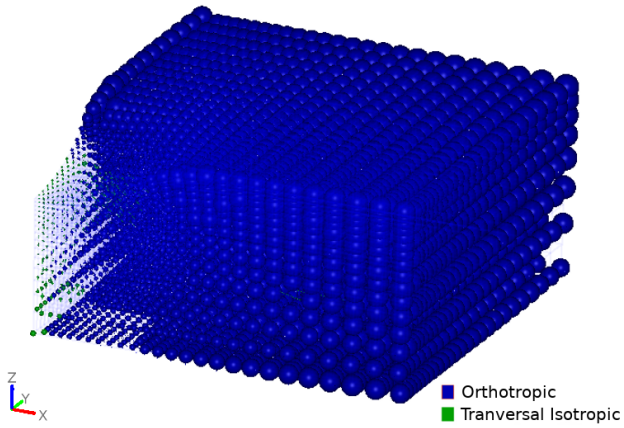

(d) Compliance $\mathrm{E}^{-1}(\mathbb{C}^{-1})$: Scaled by the factor 0.05.

Fig. 14: Indentation test: Glyph designed by Hergl et al. (2019). The length of the tubes is given in MPa for the glyphs describing the stiffness and in MPa^{-1} for the glyphs describing the compliance.

The single symmetry plane normals in the transversally isotropic indentation zone follow the principal stretch directions. Furthermore, one of the symmetry plane normals in the orthogonal area is oriented in this direction as well. Figure 14a and Figure 14c display the glyph representing the stiffness of the material. It can be recognized that the glyphs in the region close to the indentation center are bigger than in the rest of the field. Thus, the material near the indentation point is indeed stiffer. As can be seen in Figure 14a and Figure 14b, the differences in the stiffness/compliance are highlighted more in the glyphs using the compliance tensor depicted in Figure 14c and Figure 14d. Note that Figure 14b and Figure 14d use a uniaxial compliance instead of a stiffness measure.

5.2.4 Uniaxial Elasticity Glyph

The indentation test visualized by the elasticity glyph (cf. e. g. Böhlke and Brüggemann, 2001; Lago, 2017) is shown in Figure 15. All four figures show that the glyphs differ in the region of indentation from the glyphs in the other regions. Within the zone of indentation, the glyphs clearly show rotational symmetry w. r. t. the normal vector of the deformed surface. This corresponds to transversally isotropic or nearly transversally isotropic material behavior. The exact symmetries can be determined by analyzing single glyphs. Figure 15a and Figure 15c display the glyphs representing a stiffness measure of the material, Figure 15b and Figure 15d display the glyphs representing a compliance measure of the material.
The glyphs based on the stiffness tensor (Figure 15a, Figure 15b) are nearly spherical. Only the color coding can tell that the shape differs from a sphere. The glyphs representing a uniaxial stiffness (Figure 15a, Figure 15c) are bigger in the indentation zone, showing the deformation-induced stiffening of the material. These differences can be recognized easier in the figures that use the compliance tensor for the calculations (Figure 15c, Figure 15d). In these cases the glyphs near the indentation center strongly differ from a sphere. In Figure 15c, where the stiffness measure E_α is displayed, the glyphs in this zone are bigger than in the rest of the

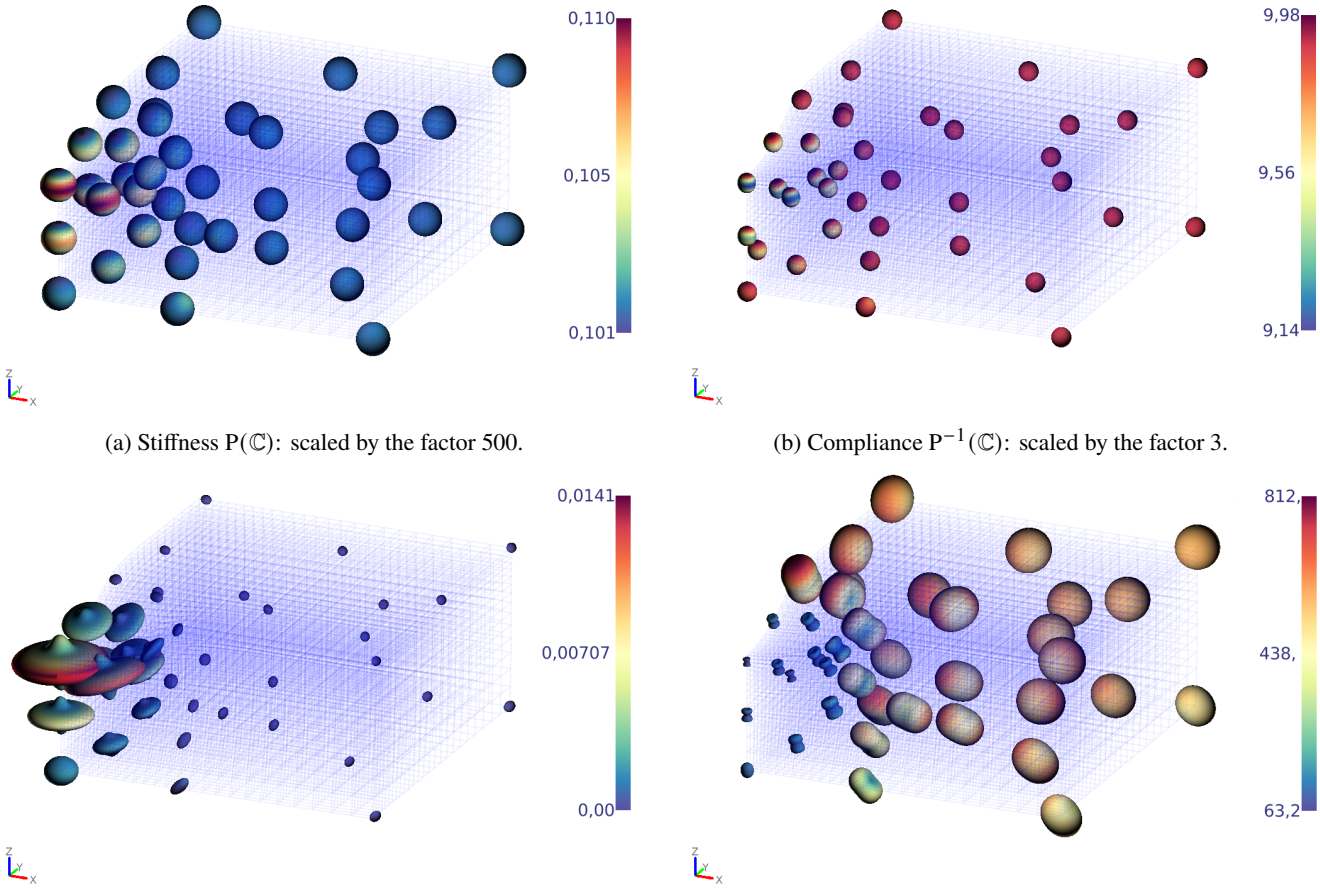

(a) Stiffness $\mathrm{P}(\mathbb{C})$: scaled by the factor 500.

(b) Compliance $\mathrm{P}^{-1}(\mathbb{C})$: scaled by the factor 3.

(c) Stiffness $\mathrm{E}(\mathbb{C}^{-1})$: scaled by the factor 10000.

(d) Compliance $\mathrm{E}^{-1}(\mathbb{C}^{-1})$: scaled by the factor 0.2.

Fig. 15: Indentation test: Glyph visualizing the stiffness/compliance of the material, described by Böhlke and Brüggemann (2001) or Lago (2017). The color legend is given in the unit Pa.

tensor field. It can be seen that the E_α is highest perpendicular to the indentation direction. Figure 15d displays the inverse glyphs representing the compliance. We note that the stiffening in the region of indentation is much more obvious in the glyphs based on the compliance (Figure 15c, Figure 15d) than in the glyphs based on the stiffness tensor (Figure 15a, Figure 15b).

6 Conclusion

This section will discuss the benefits of the different glyphs, first concerning the two examples and then in general. The four glyphs display various features. In the following, we will discuss the use of the four presented glyphs for different scenarios. The represented examples differ in dimension (2D vs. 3D), physics (elasto-plasticity vs. hyperelasticity), non-linearity (physical vs. physical & geometric), mathematical properties (singular vs. regular) and background (metal forming vs. biomechanics). We thus think they are sufficiently broad for illustrating the physical concepts behind the glyphs. We cannot choose the best out of the four glyphs because each glyph has its benefits. Which glyph to pick for a particular tensor field example is highly dependent on the application. This work presents different visualization methods to support the selection process of which visualization method to choose for a specific application.

In the analytical elasto-plastic example, the underlying plastic instability makes the stiffness tensor singular. Due to the special structure of this stiffness tensor, floating point errors in the coefficients evoke a regularization. However, calculating the inverse numerically is still a highly unstable operation. The greatest impact of this was found for the glyph designed by Hergl et al. (2019) and the elasticity glyph (cf. e. g. Böhlke and Brüggemann, 2001; Lago, 2017). Thus, for these two glyphs, it is essential to analyze whether the inverse exists or not before visualizing or interpreting the data. It must also be noticed that the (usual) limited precision in the data will not always cause these effects. As an advantage, the results of these glyphs do not require specialist knowledge. Further, it can be recognized that the glyphs calculated from the stiffness tensor are more uniform in their scaling because there is no inverse involved. However, the differences in the elasticity are highlighted more by the glyph using the compliance tensor. In contrast, interpreting the glyph designed by Neeman et al. (2008) requires knowledge about Reynold glyphs and different deformation modes. The glyph designed by Kriz et al. (2005) requires knowledge about plane wave types, i. e. in particular an imagination of the directions of propagation and oscillation. Being familiar with these concepts, the interpretation of the glyphs comes as an advantage. In addition, this glyph seems robust concerning material instability, i. e. singular stiffness tensors. Further, symmetries, as well as contrasts in stiffness, are visualized in a clear way. The analytical example also contains isotropic regions, which are represented in different ways: The glyph designed by Neeman et al. (2008) depicts the Reynolds glyph for the *smallest* eigenvalue of the stretch part of the stiffness tensor, which is not necessarily easily associated with isotropy. Moreover, the glyph is

oriented by any global coordinate system because an isotropic tensor does not contain directional information. This effect cannot be distinguished from an actual material alignment with the global coordinate system and might be misinterpreted without a more detailed analysis.
The glyphs designed by Neeman et al. (2008), Kriz et al. (2005) and the elasticity glyph (cf. e. g. Böhlke and Brüggemann, 2001; Lago, 2017) are more complex than the glyph designed by Hergl et al. (2019) and more useful for fewer data points. However, all four glyphs highlight the strongly deformed region in the indentation test in varying degrees, which is the interesting aspect of this data set. Both the symmetry type and the orientation of the material can be analyzed using each of the glyph representations.
The glyph proposed by Neeman et al. (2008) was designed to analyze deformation modes. Therefore, the eigenvalue problem is solved for the stretch part of the stiffness tensor. Neeman et al. analyzed only the eigentensor corresponding to the smallest eigenvalue in order to highlight softer regions and analyze the most compliant material points. For other applications, it can be helpful to analyze all six deformation modes, which was done in this work.
The glyph designed by Kriz et al. (2005) represents the three plane waves of the material. The representation of all three glyphs in one view contains much data while showing all glyphs in different views requires three views. The glyph designed by Neeman et al. (2008) reduces the information by choosing one eigentensor field and visualizing it in one view. Representing all six eigentensors also requires multiple views. In contrast to this, the glyph designed by Hergl et al. (2019) and the elasticity glyph (cf. e. g. Böhlke and Brüggemann, 2001; Lago, 2017) visualize all information in a single view. Whether a single view or a multiple view is preferred must be adapted to the respective situation.
The interpretation of the results of the glyph designed by Hergl et al. (2019) is intuitive, but the anisotropy types must be known. As can be seen in the indentation example, it was designed to gain an overview of symmetries occurring in extensive stiffness tensor fields and is not intended for an in-depth analysis. The anisotropy types, as well as the symmetries, can be gained from the representation, but the deviation to symmetry types other than isotropy is missing.
The elasticity glyph (cf. e. g. Böhlke and Brüggemann, 2001; Lago, 2017) is often used in the application domain. It is easy to interpret and contains essential information about the anisotropy of the material. The anisotropy type and its orientation can be determined from the form of the glyph. However, it requires an in-depth analysis of the single glyphs because small changes of the elasticity or changes of the anisotropy type are not easy to recognize.
Overall, it can be stated that every glyph has its area of application, and the most suitable choice strongly depends on the prior knowledge of the applicant. The authors of this paper will, as mentioned before, not give a recommendation of which glyph to choose. Nevertheless, we summarize the strengths of the four glyphs:

- Glyph by Neeman et al. (2008): analysis of different deformation modes;
- Glyph by Kriz et al. (2005): analysis of plane waves in each direction;
- Glyph by Hergl et al. (2019): many data points, overview of a large field;
- Elasticity Glyph (cf. e. g. Böhlke and Brüggemann, 2001; Lago, 2017): detailed analysis of single points.

Also, in some cases, the analysis of different glyphs is helpful to obtain complementary information on the stiffness tensor field. The glyph should be chosen with care to extract the relevant information from the tensor in a reliable way, especially if it is singular. The presented results can be helpful for analyzing other sorts of material instabilities.

References

Thomas Böhlke and C Brüggemann. Graphical representation of the generalized Hooke's law. *Technische Mechanik*, 21(2): 145–158, 2001.

B Ellis, G Ateshian, and J Weiss. Febio: finite elements for biomechanics. *J Biomech Eng*, 134(1):5–11, 2012.

Salvatore Federico and T. Christian Gasser. Nonlinear elasticity of biological tissues with statistical fibre orientation. *Journal of The Royal Society Interface*, 7(47):955–966, jun 2010. ISSN 1742-5689. doi: 10.1098/rsif.2009.0502. URL https://royalsocietypublishing.org/doi/10.1098/rsif.2009.0502.

Uwe-Jens Görke, Hubert Günther, Thomas Nagel, and Markus A. Wimmer. A Large Strain Material Model for Soft Tissues With Functionally Graded Properties. *Journal of Biomechanical Engineering*, 132(7):074502, 2010. ISSN 01480731. doi: 10.1115/1.4001312. URL http://biomechanical.asmedigitalcollection.asme.org/article.aspx?articleid=1426035http://www.scopus.com/inward/record.url?eid=2-s2.0-77955118459&partnerID=MN8TOARS.

R. Grytz and G. Meschke. Microstructure-oriented modeling and computational remodeling of the collagen network in corneoscleral shells. In *Computational Methods in Applied Sciences*, volume 14, pages 155–168. Springer Netherland, 2009. ISBN 9781402092305. doi: 10.1007/978-1-4020-9231-2_11. URL https://link.springer.com/chapter/10.1007/978-1-4020-9231-2_11.

Chiara Hergl, Thomas Nagel, Olaf Kolditz, and Gerik Scheuermann. Visualization of symmetries in fourth-order stiffness tensors. In *2019 IEEE Visualization Conference (VIS)*, pages 291–295. IEEE, 2019.

Chiara Hergl, Thomas Nagel, and Gerik Scheuermann. An introduction to the deviatoric tensor decomposition in three dimensions and its multipole representation. *arXiv preprint arXiv:2009.11723*, 2020.

GA Holzapfel. *Nonlinear solid mechanics, vol. 24*. Chichester, New York, 2000.

Andrea Kratz, Cornelia Auer, Markus Stommel, and Ingrid Hotz. Visualization and analysis of second-order tensors: Moving beyond the symmetric positive-definite case. In *Computer Graphics Forum*, volume 32, pages 49–74. Wiley Online Library, 2013.

RD Kriz, M Yaman, M Harting, and AA Ray. Visualization of zeroth, second, fourth, higher order tensors, and invariance of tensor equations. *Computers and Graphics*, 21(6):1–13, 2005.

Bc Dušan Lago. Effective tool for material elasticity computation. *Master's Thesis. Brno, Spring*, 2017.

Morteza M. Mehrabadi and Stephen C. Cowin. Eigentensors of linear anisotropic elastic materials. *The Quarterly Journal of Mechanics and Applied Mathematics*, 43(1):15–41, 1990. ISSN 0033-5614. doi: 10.1093/qjmam/43.1.15. URL https://academic.oup.com/qjmam/article-lookup/doi/10.1093/qjmam/43.1.15.

Kevin M Moerman, Ciaran K Simms, and Thomas Nagel. Control of tension–compression asymmetry in Ogden hyperelasticity with application to soft tissue modelling. *Journal of the Mechanical Behavior of Biomedical Materials*, 56:218–228, mar 2016. ISSN 17516161. doi: 10.1016/j.jmbbm.2015.11.027. URL http://www.scopus.com/inward/record.url?eid=2-s2.0-84951021376&partnerID=MN8TOARShttp://linkinghub.elsevier.com/retrieve/pii/S1751616115004452.

Thomas Nagel and Norbert Böttcher. *Mechanical Processes*, pages 185–201. Springer International Publishing, 2015. ISBN 978-3-319-11894-9. doi: 10.1007/978-3-319-11894-9_7.

Thomas Nagel, Uwe-Jens Görke, Kevin M. Moerman, and Olaf Kolditz. On advantages of the Kelvin mapping in finite element implementations of deformation processes. *Environmental Earth Sciences*, 75(11):937, jun 2016. ISSN 1866-6280. doi: 10.1007/s12665-016-5429-4. URL http://www.scopus.com/inward/record.url?eid=2-s2.0-84971641049&partnerID=MN8TOARShttp://link.springer.com/10.1007/s12665-016-5429-4.

Alisa G Neeman, Rebecca Brannon, Boris Jeremić, Allen Van Gelder, and Alex Pang. Decomposition and visualization of fourth-order elastic-plastic tensors. In *Proceedings of the Fifth Eurographics/IEEE VGTC conference on Point-Based Graphics*, pages 121–128, 2008.

Joachim Nordmann, Marcus Aßmus, Rainer Glüge, and Holm Altenbach. On the derivation of hooke's law for plane state conditions. *Technische Mechanik-European Journal of Engineering Mechanics*, 40(2):160–174, 2020.

Raymond William Ogden. Large deformation isotropic elasticity: on the correlation of theory and experiment for compressible rubberlike solids. *Proceedings of the Royal Society of London. Series A, Mathematical and Physical Sciences*, pages 567–583, 1972.

Giulia Scalet and Ferdinando Auricchio. *Computational Methods for Elastoplasticity: An Overview of Conventional and Less-Conventional Approaches*, volume 25. Springer Netherlands, 2018. ISBN 0123456789. doi: 10.1007/s11831-016-9208-x.

Appendix

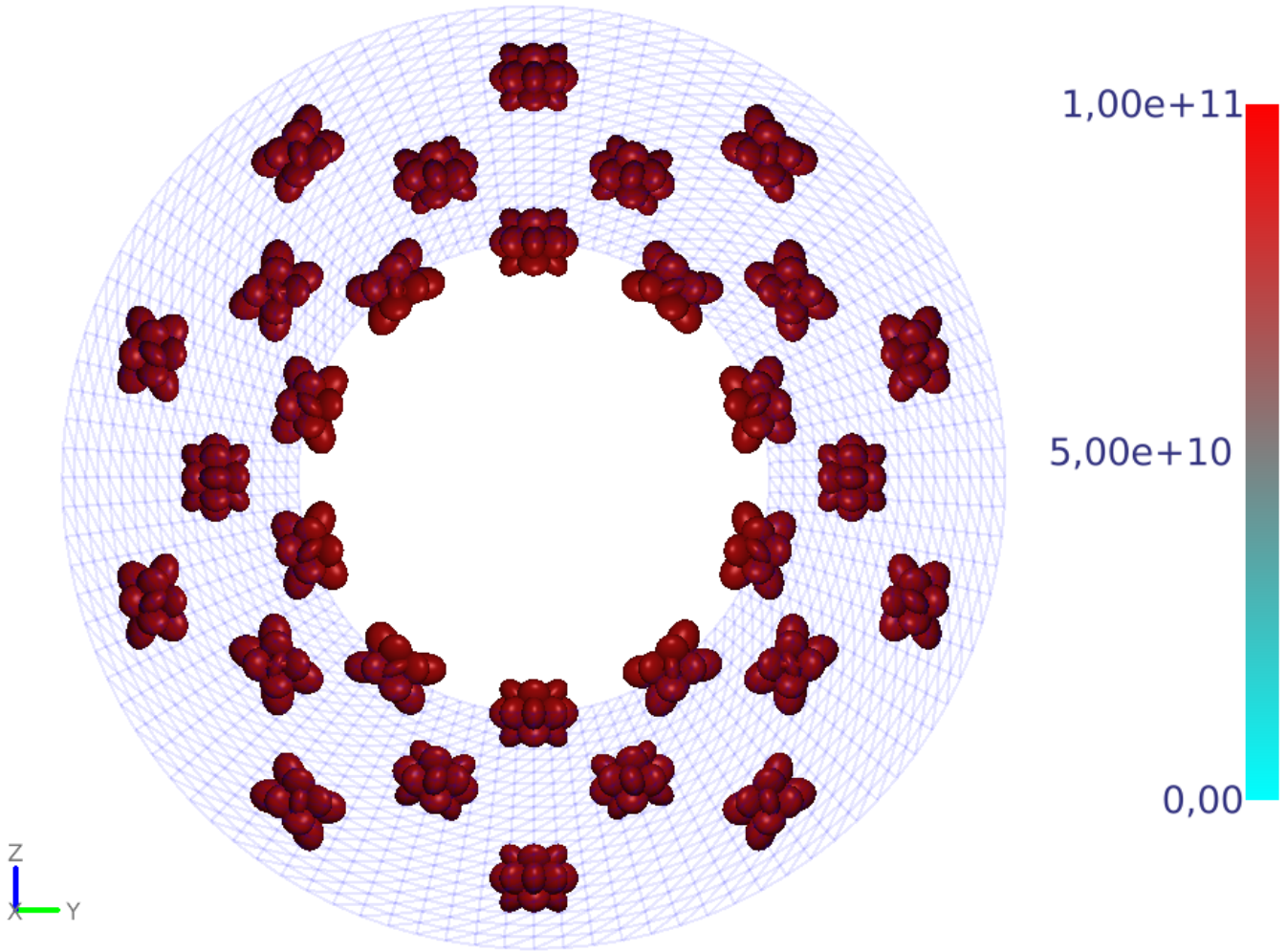

Fig. 16: Analytical example: Glyph designed by Neeman et al. (2008) corresponding to the eigenvalues two to five of the inner shell in a single view, unit Pa.

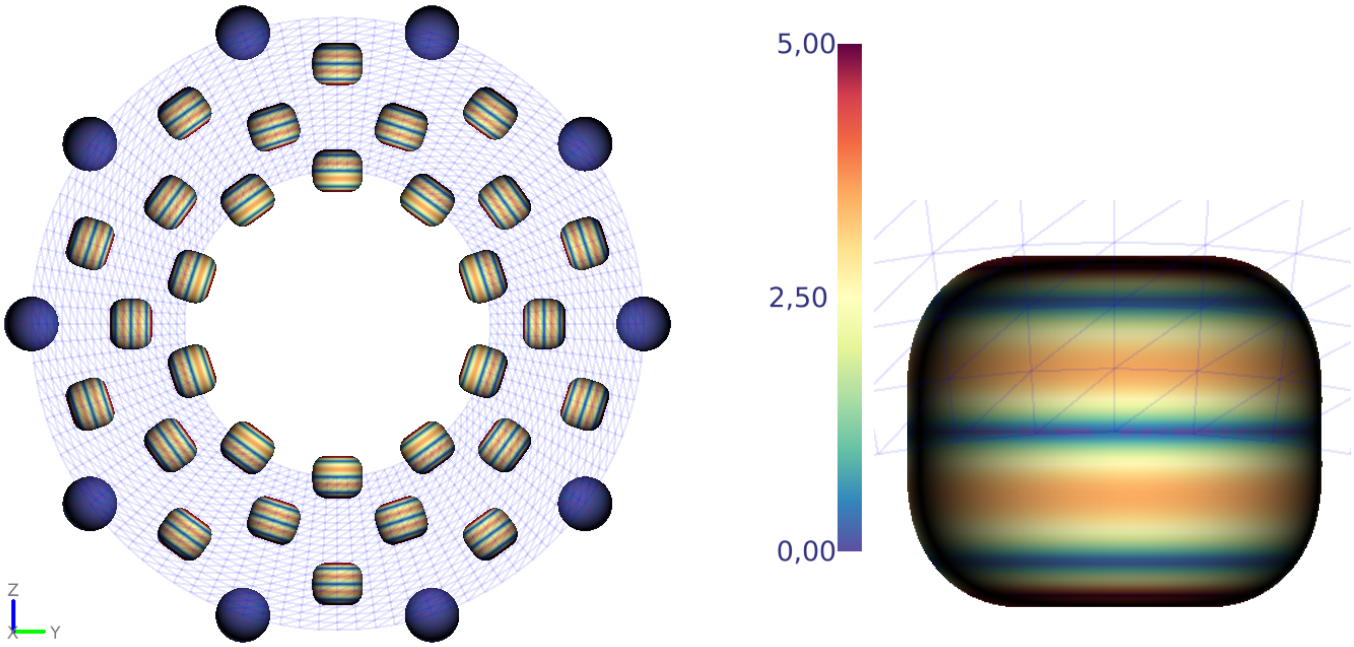

Fig. 17: Analytical example: Glyph designed by Kriz et al. (2005) representing the plane waves. Fast wave, the color depicts the polarization angle in °.

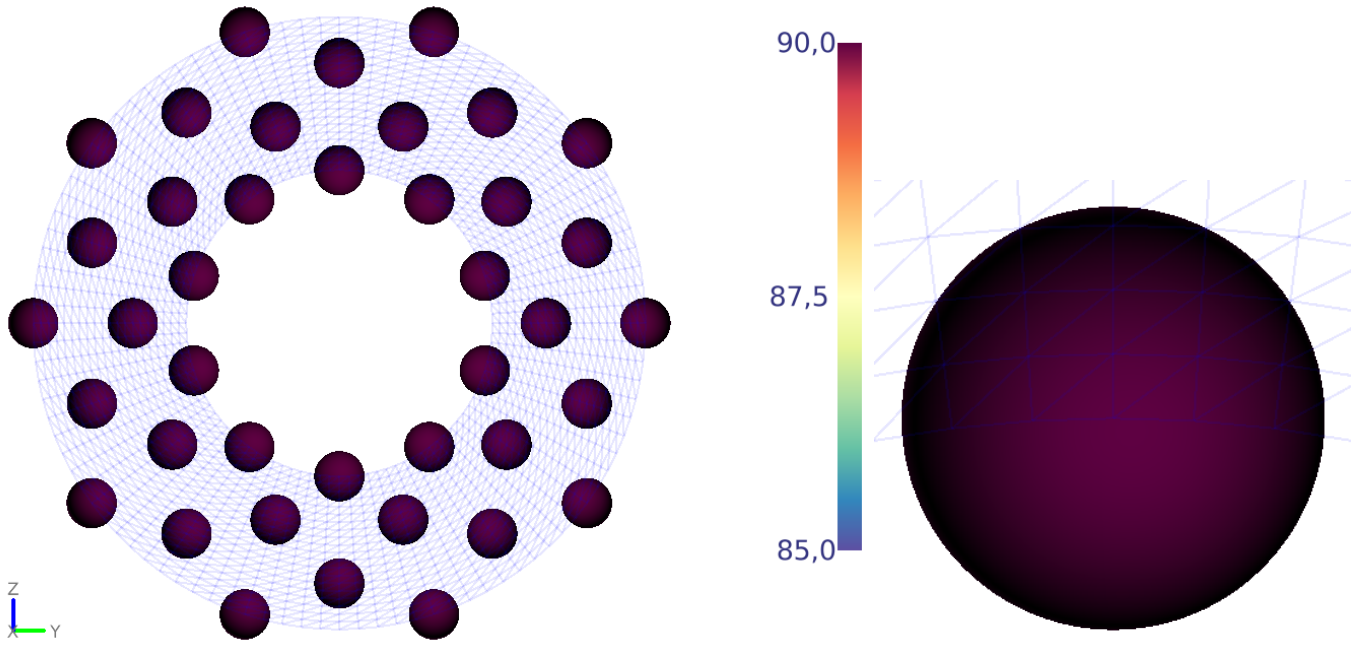

Fig. 18: Analytical example: Glyph designed by Kriz et al. (2005) representing the plane waves. Intermediate wave, the color depicts the polarization angle in °.

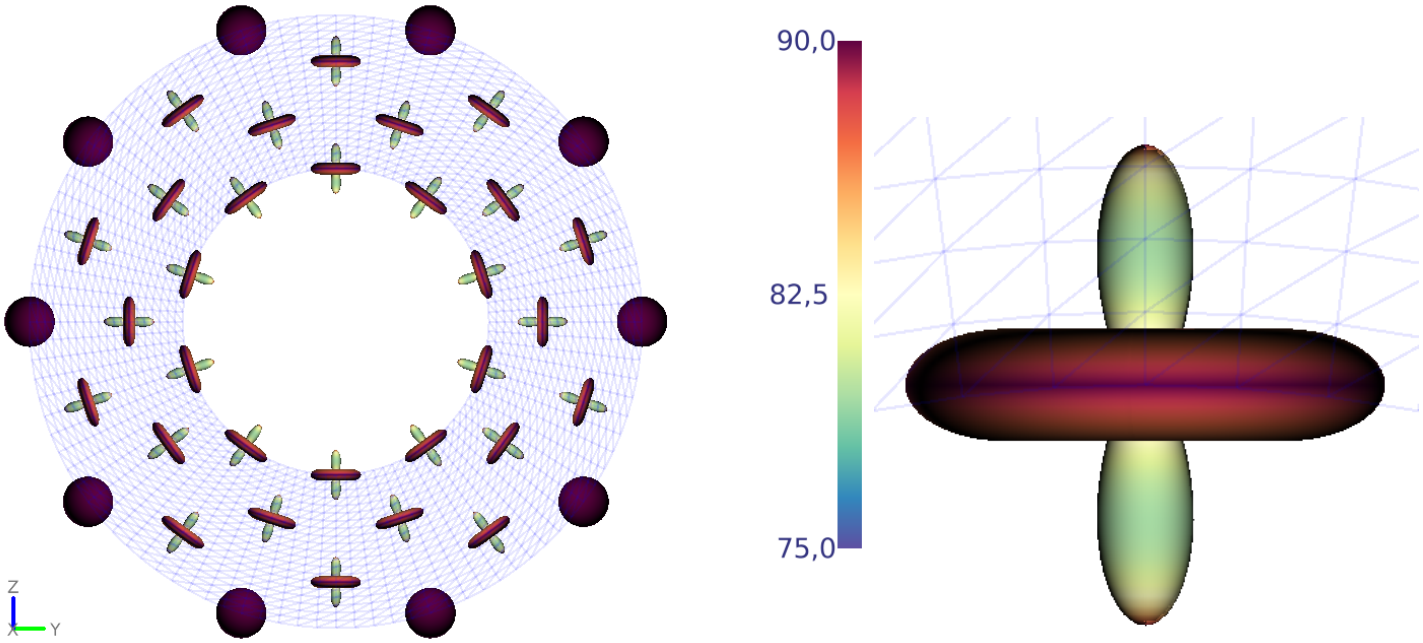

Fig. 19: Analytical example: Glyph designed by Kriz et al. (2005) representing the plane waves. Slow wave, the color depicts the polarization angle in °.

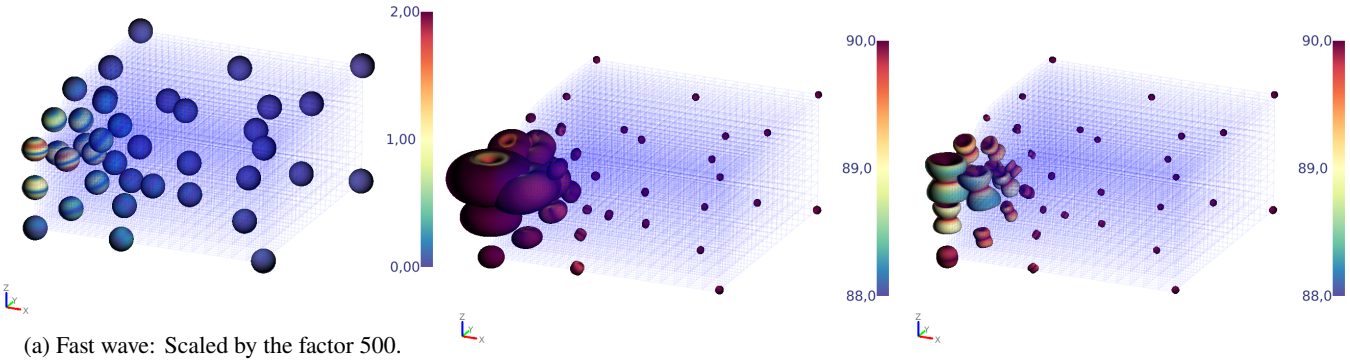

(a) Fast wave: Scaled by the factor 500.

(b) Intermediate wave: Scaled by factor 30000.

(c) Slow wave: Scaled by the factor 30000.

Fig. 20: Indentation test: Glyph designed by Kriz et al. (2005) representing the plane waves using separate color bars. The color depicts the polarization angle in °.

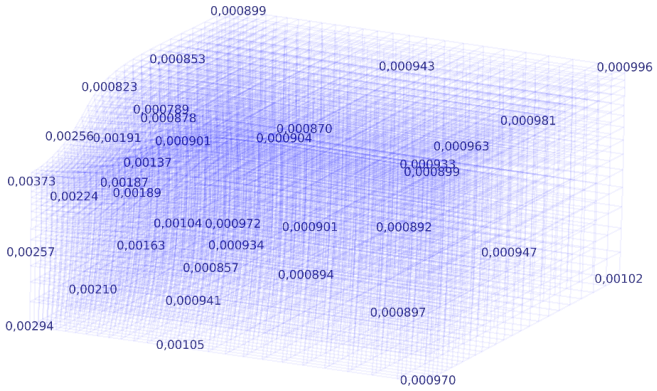

(a) First eigenvalue of the stretch part of the stiffness tensor.

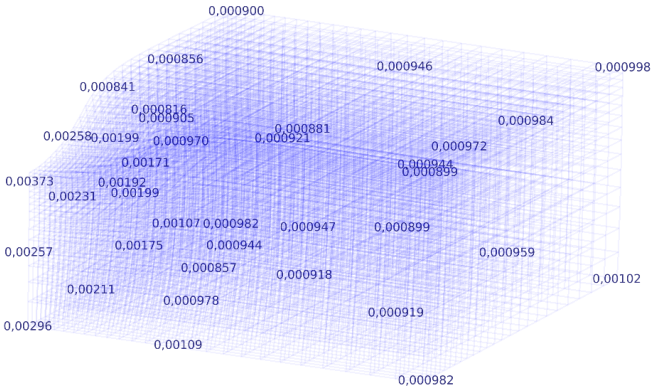

(b) Second eigenvalue of the stretch part of the stiffness tensor.

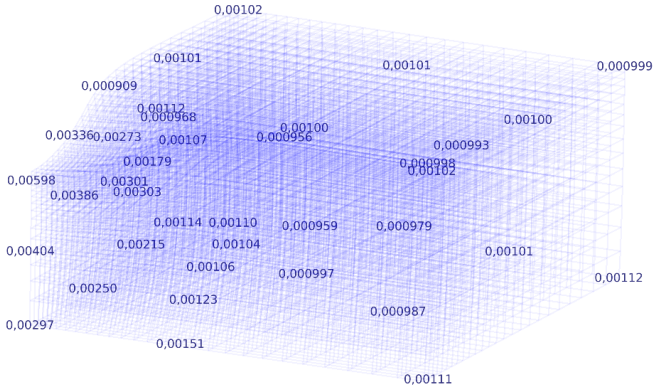

(c) Third eigenvalue of the stretch part of the stiffness tensor.

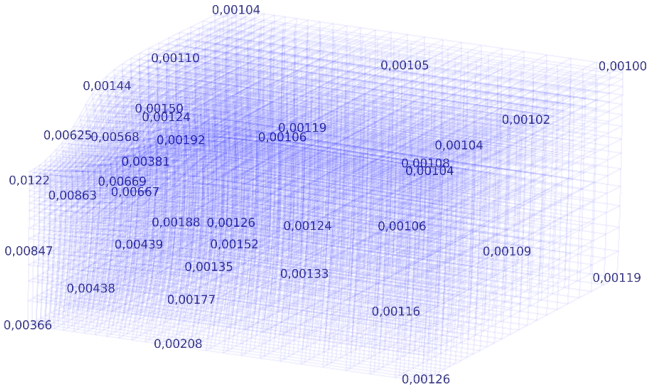

(d) Fourth eigenvalue of the stretch part of the stiffness tensor.

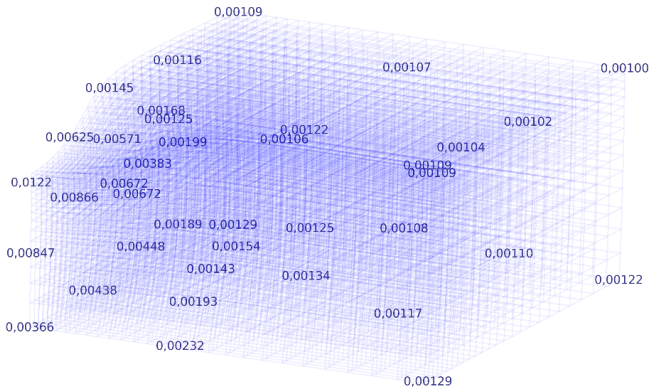

(e) Fifth eigenvalue of the stretch part of the stiffness tensor.

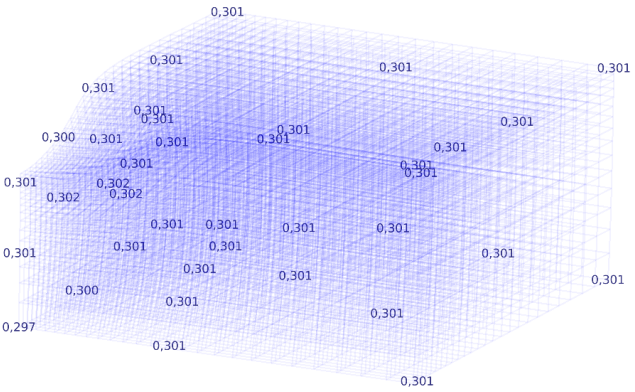

(f) Sixth eigenvalue of the stretch part of the stiffness tensor.

Fig. 21: Indentation test: Eigenvalues of the stretch part of the stiffness tensor in the unit MPa.